附件1   浙江水利水电学院"南浔学者"申请表

姓　名	杭州明	出生年月	1980 年　09 月	参加工作时间	2010 年 07 月
现所在单位(部门)	机械与汽车工程学院	最高学历/学位	研究生/博士	专业技术职务	高级工程师

拟申报类别	三类学者

符合条款	符合三类学者业绩成果（2）发表 3 类期刊论文 1 篇，绩点 50；发表 5 类期刊论文 1 篇，绩点 20。总绩点 70。

所涉业绩	教学类绩点：____	
	科研类绩点：__70__	Microstructure and hydrogen storage properties of $Ti_{10+x}V_{80-x}Fe_6Zr_4$ (x=0~15) alloys Zhouming Hang, Lixin Chen, Xuezhang Xiao, Zhendong Yao, Liqiu Shi, Yan Feng, Li Yang. Int. J. of Hydrogen Energy, 2021, 46 (54): 27622-27630.（3 类期刊论文）（SCI TOP 中科院二区）
		Enhancing Hydrogen Storage Kinetics and Cycling Properties of NaMgH3 by 2D Transition Metal Carbide MXene Ti3C2 Zhouming Hang, Zhencan Hu, Xuezhang Xiao, Ruicheng Jiang and Meng Zhang. Processes, 2021, 9(10):1690.（5 类期刊论文）（SCI 中科院三区）
	人才称号类绩点：____	
	与上述水平相当的其他业绩	
	总绩点	70

个人承诺	本人承诺上述所填内容真实、准确；如有不实，本人承担相应责任。 签名：杭州明　时间：2022.11.21

以上部分由申请人填写，所在单位审核。以下由单位（部门）和学校填写。

所在单位（部门）意见	1.经审核，申请人所填内容：□属实　　□不属实； 2.是否符合所申请的类别：□符合　□不符合； 3.是否同意推荐：□同意　□不同意。 　　　　　　　　　　　　　　　负责人签名：　　　　　（部门盖章） 　　　　　　　　　　　　　　　　　　____年___月___日

科技处审核意见	负责人签名：　　（部门盖章） 年___月___日	教务处审核意见	负责人签名：　　　（部门盖章） 年___月___日

其他相关职能部门审核意见	负责人签名：　　　　　（部门盖章） 　　　　　　　　　　　　　　　　　　____年___月___日

学校意见	（学校盖章） 　　　　　　　　　　　　　　　　____年___月___日

基本信息		☆ 登录收藏

INTERNATIONAL JOURNAL OF HYDROGEN ENERGY

INT J HYDROGEN ENERG

期刊名字

LetPub评分

7.9 ★★★☆☆ 186人评分　**我要评分** ✏

声誉		7.9
影响力		7.4
速度		7.3

微信扫码收藏此期刊

期刊ISSN	0360-3199
2021-2022最新影响因子（数据来源于搜索引擎）	注册或登录后，查看影响因子和历年趋势图
2021-2022自引率	27.20%　注册或登录后，查看自引率趋势图
h-index ⓘ	187

CiteScore ⓘ	CiteScore	SJR	SNIP	CiteScore排名			
				学科	分区	排名	百分位
	10.00	1.201	1.368	大类：Physics and Astronomy 小类：Condensed Matter Physics	Q1	28 / 415	93%
				大类：Physics and Astronomy 小类：Energy Engineering and Power Technology	Q1	23 / 235	90%
				大类：Physics and Astronomy 小类：Fuel Technology	Q1	15 / 109	86%
				大类：Physics and Astronomy 小类：Renewable Energy, Sustainability and the Environment	Q1	37 / 215	83%

期刊简介

The International Journal of Hydrogen Energy aims to provide a central vehicle for the exchange and dissemination of new ideas, technology developments and research results in the field of Hydrogen Energy between scientists and engineers throughout the world. The emphasis is placed on original research, both analytical and experimental, covering all aspects of Hydrogen Energy, including production, storage, transmission, utilization, enabling technologies, environmental impact, economic and international aspects of hydrogen and hydrogen carriers such as NH3, CH4, alcohols, etc.

The utilization includes thermochemical (combustion), photochemical, electrochemical (fuel cells) and nuclear conversion of hydrogen, hydrogen isotopes and/or hydrogen carriers to thermal, mechanical and electrical energies, and their applications in transportation (including aerospace), industrial, commercial and residential sectors.

When outstanding new advances are made, or when new areas have been developed to a definitive stage, special review articles will be considered. Shorter communications are also welcome.

期刊官方网站	http://www.elsevier.com/wps/find/journaldescription.cws_home/485/description#description
期刊投稿网址	https://www.editorialmanager.com/HE
是否OA开放访问	No
通讯方式	PERGAMON-ELSEVIER SCIENCE LTD, THE BOULEVARD, LANGFORD LANE, KIDLINGTON, OXFORD, ENGLAND, OX5 1GB
出版商	Elsevier Ltd
涉及的研究方向	工程技术-环境科学
出版国家或地区	ENGLAND
出版语言	English
出版周期	Semimonthly
出版年份	1976
年文章数 ⓘ	3312　注册或登录后，查看年文章数趋势图
Gold OA文章占比	2.63%
研究类文章占比：文章 ÷（文章＋综述）	95.02%

WOS期刊SCI分区 ⓘ
（**2021-2022年最新版**）

WOS分区等级：2区

按学科分区	
ENERGY & FUELS	Q2
CHEMISTRY, PHYSICAL	Q2
ELECTROCHEMISTRY	Q2

中科院《国际期刊预警名单（试行）》名单 ⓘ

2021年12月发布的2021版：不在预警名单中

2021年01月发布的2020版：不在预警名单中

中科院SCI期刊分区
（**2021年12月最新基础版**）

注册或登录后，查看中科院SCI期刊分区趋势图

大类学科		小类学科		Top期刊	综述期刊
工程技术	2区	CHEMISTRY, PHYSICAL 物理化学	3区	是	否
		ELECTROCHEMISTRY 电化学	3区		
		ENERGY & FUELS 能源与燃料	3区		

中科院SCI期刊分区
（**2021年12月最新升级版**）ⓘ

大类学科		小类学科		Top期刊	综述期刊
工程技术	2区	ELECTROCHEMISTRY 电化学	2区	是	否
		CHEMISTRY, PHYSICAL 物理化学	3区		
		ENERGY & FUELS 能源与燃料	3区		

中科院SCI期刊分区
（**2020年12月旧的升级版**）

大类学科		小类学科		Top期刊	综述期刊
工程技术	2区	ELECTROCHEMISTRY 电化学	2区	是	否
		CHEMISTRY, PHYSICAL 物理化学	3区		
		ENERGY & FUELS 能源与燃料	3区		

《SCI-EXPANDED》收录及《JCR》期刊影响因子、分区情况证明

经检索《Web of Science》和《Journal Citation Reports（JCR）》数据库，《Science Citation Index Expanded (SCI-EXPANDED)》收录论文及其期刊影响因子、分区情况如下。（检索时间：2021 年 9 月 6 日）

第 1 条，共 1 条

标题:Microstructure and hydrogen storage properties of Ti10+xV80-xFe6Zr4 (x=0 similar to 15) alloys

作者:Hang, ZM(Hang, Zhouming);Chen, LX(Chen, Lixin);Xiao, XZ(Xiao, Xuezhang);Yao, ZD(Yao, Zhendong);Shi, LQ(Shi, Liqiu);Feng, Y(Feng, Yan);Yang, L(Yang, Li);

来源出版物:INTERNATIONAL JOURNAL OF HYDROGEN ENERGY 卷:46 期:54 页:27622-27630

DOI:10.1016/j.ijhydene.2021.06.019 出版年:AUG 5 2021

入藏号:WOS:000677990300015

文献类型:Article

地址:[Hang, Zhouming; Shi, Liqiu; Feng, Yan] Zhejiang Univ Water Resources & Elect Power, Zhejiang Engn Res Ctr Adv Hydraul Equipment, Hangzhou 310018, Peoples R China.

[Chen, Lixin; Xiao, Xuezhang; Yao, Zhendong] Zhejiang Univ, Sch Mat Sci & Engn, Hangzhou 310027, Peoples R China.

[Hang, Zhouming; Shi, Liqiu; Feng, Yan] Zhejiang Univ Water Resources & Elect Power, Key Lab Technol Rural Water Management Zhejiang P, Hangzhou 310018, Peoples R China.

[Hang, Zhouming; Shi, Liqiu; Feng, Yan] Zhejiang Univ Water Resources & Elect Power, Coll Mech & Automot Engn, Hangzhou 310018, Peoples R China.

[Yang, Li] Zhejiang Univ Water Resources & Elect Power, Coll Elect Engn, Hangzhou 310018, Peoples R China.

通讯作者地址:

Hang, ZM (corresponding author), Zhejiang Univ Water Resources & Elect Power, Zhejiang Engn Res Ctr Adv Hydraul Equipment, Hangzhou 310018, Peoples R China.; Hang, ZM (corresponding author), Zhejiang Univ Water Resources & Elect Power, Key Lab Technol Rural Water Management Zhejiang P, Hangzhou 310018, Peoples R China.; Hang, ZM (corresponding author), Zhejiang Univ Water Resources & Elect Power, Coll Mech & Automot Engn, Hangzhou 310018, Peoples R China.

电子邮件地址:hangzhm@zjweu.edu.cn

IDS 号:TQ0OX

ISSN:0360-3199

eISSN:1879-3487

期刊《INT J HYDROGEN ENERG》2020 年的影响因子为 5.816，五年影响因子为 5.242。

期刊《INT J HYDROGEN ENERG》2020 年的 JCR 分区情况为:

Edition	JCR® 类别	类别中的排序	JCR 分区
SCI	ELECTROCHEMISTRY	9/29	Q2
SCI	CHEMISTRY, PHYSICAL	48/162	Q2
SCI	ENERGY & FUELS	37/114	Q2

注：1. 期刊影响因子及分区情况最新数据以 JCR 数据库最新数据为准。
2. 以上检索结果来自 CALIS 查收查引系统。
3. 以上检索结果均得到委托人及被检索作者的确认。
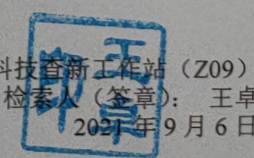
教育部科技查新工作站（Z09）
检索人（签章）：王卓
2021 年 9 月 6 日

1
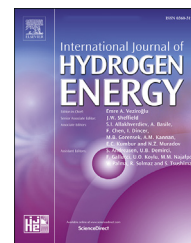
Microstructure and hydrogen storage properties of Ti$_{10+x}$V$_{80-x}$Fe$_6$Zr$_4$ (x=0~15) alloys

Check for updates

Zhouming Hang [a,c,d,*], Lixin Chen [b], Xuezhang Xiao [b], Zhendong Yao [b], Liqiu Shi [a,c,d], Yan Feng [a,c,d], Li Yang [e]

[a] Zhejiang Engineering Research Center for Advanced Hydraulic Equipment, Zhejiang University of Water Resources and Electric Power, Hangzhou, 310018, China
[b] School of Materials Science and Engineering, Zhejiang University, Hangzhou, 310027, China
[c] Key Laboratory for Technology in Rural Water Management of Zhejiang Province, Zhejiang University of Water Resources and Electric Power, Hangzhou, 310018, China
[d] College of Mechanical and Automotive Engineering, Zhejiang University of Water Resources and Electric Power, Hangzhou, 310018, China
[e] College of Electrical Engineering, Zhejiang University of Water Resources and Electric Power, Hangzhou, 310018, China

HIGHLIGHTS

- Bulk Ti$_{10+x}$V$_{80-x}$Fe$_6$Zr$_4$ (x = 0, 5, 10, 15) are directly used into the activation.
- The incubation time for activation for Ti$_{15}$V$_{75}$Fe$_6$Zr$_4$ is only 12 s.
- The substitution of Ti for V within 10 at.% enhances the absorption capacity.

ARTICLE INFO

ABSTRACT

The microstructure and hydrogen storage properties of Ti$_{10+x}$V$_{80-x}$Fe$_6$Zr$_4$ (x = 0, 5, 10, 15) alloys have been studied. XRD and SEM analyses show that all alloys consist of a BCC main phase and a small fraction of C14 Laves secondary phase, in which the latter precipitates along the grain boundary of the former becoming network structure. With increasing Ti content in the alloy, the lattice parameter and cell volume of the BCC main phase of the alloy increase. The chemical composition of each phase is analysed by EDS, from which the lattice parameters of BCC phase have a good linear relationship with their average atomic radii. All bulk alloys have good activation behaviors and hydriding kinetics. With the increase of Ti content, the incubation time for activation decreases first and then increases under an initial hydrogen pressure of 4 MPa at 298 K. The incubation time of Ti$_{15}$V$_{75}$Fe$_6$Zr$_4$ alloy is only 12 s. It is one of the shortest incubation time in V-based solid solution alloys as far as we know, which may be related to the existence of C14 Laves phase. All the alloys have relatively high hydrogen absorption capacities of above 3 wt%, which increase first and then decrease as the Ti content increases, achieving the maximum capacity of 3.61 wt % at x = 10 at 298 K. With increasing x, the equilibrium plateau pressure of dehydrogenation of the samples at 353 K decreases owing to the expansion of unit cell of main phase, which is far below 0.1 MPa for x = 10 and 15. The maximum desorption capacity of 1.94 wt%

(desorbed to 0.001 MPa) is obtained at $x = 5$, compared to that of 1.6 wt% (desorbed to 0.1 MPa) achieved at $x = 0$.

Introduction

Energy is the lifeblood of national economy and the source of human social activities. Clean environment is the basis of sustainable development of human society. Among various categories of new energy carriers, hydrogen is regarded as one of the most promising energy due to nearly no pollutant emission. Compared with the liquid and gaseous hydrogen storage, storing hydrogen in a solid state has advantages in security and high volumetric capacity.

In the latest research, hydrogen storage properties of different types of materials were reported in literature [1–3], such as $AB_{3.42}$-type La–Y–Ni based alloy, La_2Mg_{17}/Ni system and AlH_3. However, For $AB_{3.42}$-type La–Y–Ni based alloys, only the low temperature electrochemical properties are studied through element substitution and surface treatment, while the gas-solid hydrogen storage characteristics were not mentioned. For La_2Mg_{17}/Ni system, Although hydrogen storage capacities and cycle stabilities of La_2Mg_{17}/Ni system increased due to special surface stratified configuration, dehydrogenation temperatures were still too high (above 550 K). AlH_3 contains a high volumetric and gravimetric energy density, but direct hydrogenation of bulk Al into AlH_3 requires hydrogen pressures as high as several GPas and the reversibility of nanoconfined AlH_3 also needs to be further confirmed. Consequently, the alloys mentioned above are far from practical application.

V-based solid solution alloys have been widely concerned for their theoretical hydrogen storage capacity of about 3.8 wt % [4,5] and good dynamic performance. Nevertheless, the disadvantages of difficult in activation, high cost and low hydrogen release at ambient temperature restrict the practical application of the alloys.

A large number of studies have demonstrated that multi-alloying could effectively improve the comprehensive properties of V-based hydrogen storage alloy [4,6–20]. Challet et al. [7] studied the structure and hydrogen storage performance of $(Ti_{0.355}V_{0.645})_{100-x}Fe_x$ ($x = 7$, 14), of which the hydrogen absorption capacity at 298 K was 3.95 wt% and 3.8 wt% respectively. The reversible capacity of $(Ti_{0.355}V_{0.645})_{93}Fe_7$ alloy is only 0.33 wt% at 298 K. When the temperature rises to 573 K, the reversible capacity suddenly rises to 3.18 wt%. Our previous study found that the addition of Zr element can significantly improve the activation performance of Ti–V–Fe hydrogen storage alloy and the optimal overall hydrogen storage performance is obtained for $Ti_{10}V_{80}Fe_6Zr_4$ [9]. On the basis of this study, the microstructure and hydrogen storage performance of $Ti_{10+x}V_{80-x}Fe_6Zr_4$ ($x = 0$, 5, 10, 15) system alloys were investigated systematically in

this paper for reducing the alloy cost (the price of Ti is much lower compared with V) and further improving its overall hydrogen storage performance.

Experimental

The $Ti_{10+x}V_{80-x}Fe_6Zr_4$ ($x = 0$, 5, 10, 15) alloy samples were prepared by levitation induction melting under argon atmosphere and remelted for four times to ensure high homogeneity. All starting elemental metals of V, Ti, Zr and Fe have purity higher than 99%. The crystal structures of the samples were studied by X-ray diffraction (XRD) using Cu Kα radiation. The morphology and elemental distribution of the samples were examined by using a scanning electron microscope (SEM) and an energy dispersive X-ray spectrometer (EDS), respectively.

For activation measurement, a bulk sample with 4 g was loaded in a reactor and evacuated for 15 min at 298 K using a rotary pump, then high-purity hydrogen was introduced gradually into the reactor up to 4 MPa for the hydriding process. Activation refers to the process in which the sample reaches its maximum hydrogen absorption capacity. Then, the reactor was evacuated for 30 min at 673 K for the next hydriding process. In this study, the hydrogen absorption capacity is defined as the hydrogen content under a pressure of 4 MPa at 298 K. Hydrogen storage behaviors were conducted on a Sievert's type apparatus (MH-008), which performed well in air tightness.
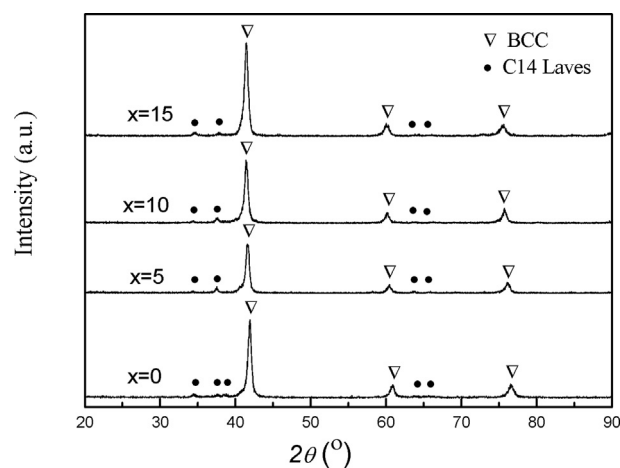
Fig. 1 – XRD patterns of as-cast $Ti_{10+x}V_{80-x}Fe_6Zr_4$ ($x = 0$~15) alloys.

Results and discussion

Microstructure

The XRD patterns of $Ti_{10+x}V_{80-x}Fe_6Zr_4$ ($x = 0$, 5, 10, 15) alloys are shown in Fig. 1. All alloys are composed of V-based BCC main phase and a small amount of C14 Laves secondary phase, of which diffraction peaks are not noticeable in the patterns due to the relatively low abundance. With the increase of Ti content, the diffraction peaks of the BCC phase shift to the left (low angle direction), due to the larger atomic radius of Ti (1.47 Å) than that of V (1.32 Å). The increase of Ti content in the alloy would increase the lattice parameter and cell volume of the BCC phase. The crystal characteristics of the BCC phases and phase abundance of each phase in the alloys are determined by Rietveld refinement and the results are listed in Tables 1 and 2.

The SEM micrographs of $Ti_{10+x}V_{80-x}Fe_6Zr_4$ ($x = 0$, 5, 10, 15) alloys are shown in Fig. 2. It can be seen that all of these alloys are made up of a main phase (dark region) and a secondary phase (bright region). The secondary phase precipitates along the grain boundary of the main phase and forms a network structure. Evidently, the amount of dark region for each alloy is much higher than that of bright region. Therefore, it is reasonable for this type of alloys to deduce that the dark region is the BCC main phase and the bright region is the C14 Laves secondary phase through SEM observation together with XRD analysis (Fig. 1), which is in good agree with literature [6,21−23].

However, it seems that the network of bright phase in the alloys with $x = 0$ and 15 is quite connected, while it is discrete for $x = 5$ and 10. The reason is probably the variation of cooling rate within the ingot during solidification, resulting in the formation of equiaxed or columnar grain for main phase [24]. It is well known that equiaxed structure is supposed to be uncompacted enough after solidification, which would easily leads to intergranular precipitation of the bright phase as observed in Fig. 2(a) and (d). On the contrary, the relatively high compactness of the columnar structure may make the intergranular precipitation slightly more difficult as displayed in Fig. 2(b) and (c). On this account, the variation in relative amount of secondary phase with Ti content is difficult to estimate from these SEM images, compared with the determination of phase abundance by Rietveld refinement from XRD patterns.

The EDS mappings of $Ti_{15}V_{75}Fe_6Zr_4$ alloy are shown in Fig. 3. It can be seen that the difference of Ti content in BCC and C14 Laves phase is not obvious, and the content of Fe in C14 Laves phase is slightly higher than that in BCC phase. While the distribution of V in BCC phase is much higher than that in C14 Laves phase. In sharp contrast, Zr element is almost completely distributed in C14 Laves phase with

Table 1 − The crystal characteristics of BCC phase of $Ti_{10+x}V_{80-x}Fe_6Zr_4$ ($x = 0~15$) alloys.

Sample (x)	0	5	10	15
Lattice parameter, a (nm)	0.30437	0.30617	0.30761	0.30786
Cell volume, V (nm^3)	0.02820	0.02870	0.02911	0.02918

Table 2 − The phase abundance (wt.%) of each phase in $Ti_{10+x}V_{80-x}Fe_6Zr_4$ ($x = 0~15$) alloys.

Sample (x)	0	5	10	15
BCC	92.62	86.8	88.7	92.3
C14	7.38	13.2	11.2	7.7

depletion in BCC phase. It seems that BCC phase could not accommodate the Zr, forcing the formation of C14 Laves phase. This finding is in line with literature [9,11,13,16,24−26].

The EDS results of $Ti_{10+x}V_{80-x}Fe_6Zr_4$ ($x = 0$, 5, 10, 15) alloys are presented in Table 3, and the elemental distribution in the two phases of each alloy is basically consistent with the EDS mapping results of $Ti_{15}v_{75}Fe_6Zr_4$ alloy.

Based on the data presented in Tables 1 and 3, the variations of lattice parameter and average atomic radius of BCC phase with Ti content are plotted in Fig. 4. It can be seen that the lattice parameter increases linearly with the rise in Ti content from $x = 0$ to $x = 10$ as well as that in average atomic radius. However, as the Ti content further increases to $x = 15$, the increase in the lattice parameter is not linear with the increase in Ti content but distinctly smaller than that of the linear tendency, which may be attributed to the similar change in the average atomic radius. Meanwhile, the lattice parameter is plotted as a function of the average atomic radius in Fig. 5, in which a linear relationship between the lattice parameter and average atomic radius of the BCC phase in the alloys is evident, further confirming the variation law displayed in Fig. 4.

Activation behaviors and hydrogen absorption/desorption properties

The activation hydriding curves of $Ti_{10+x}V_{80-x}Fe_6Zr_4$ ($x = 0$, 5, 10, 15) alloys are shown in Fig. 6. It is found that all the alloys have been activated in the first hydrogenation process. The incubation times of all the alloys are listed in Table 4. With the increase of Ti content, the incubation time of the alloy decreases first and then increases, achieving the minimum value of 12 s for the alloy with $x = 5$, which indicates that the best activation performance of the alloy is obtained at $x = 5$. It also can be seen that all the alloys achieve the maximum capacities within a short time after the incubation period, reflecting the remarkable hydriding kinetics.

It was reported that the C14 Laves phase (secondary phase) is responsible for the easy activation of the V-based alloys [11,13,26]. In this study, as displayed in Table 2, the phase abundance of C14 Laves phase increases first and then decreases, attaining the maximum content of 13.2 wt% at $x = 5$. It could well explain why the alloy with $x = 5$ shows the best activation performance.

For the activation of V-based solid solution alloys, it is common for the alloys to withstand the harsh pretreatment (high pressure and high temperature) [27,28]. However, the alloys in this study could complete the activation during the first hydrogenaiton with the incubation time of no more than 34 min, which were only subjected to the pretreatment of evacuation of 15 min at 298 K. Even then, the activation behaviors are also enhanced to certain extent, compared to incubation times of 1600 s and 120 min for Ti−32 V−10Cr−18Mn
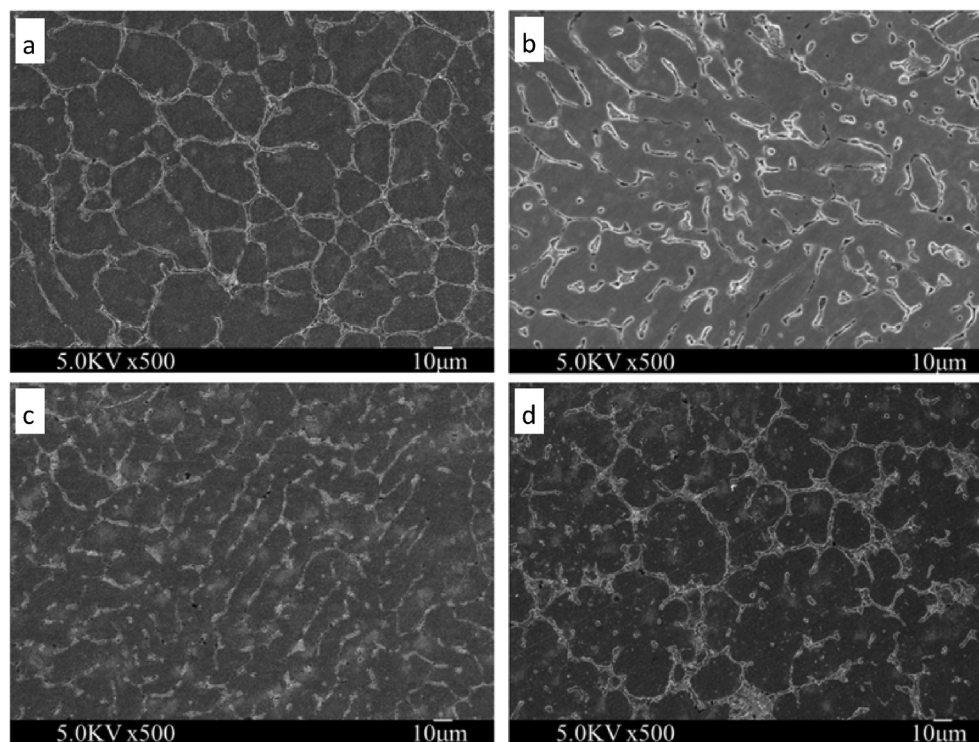
Fig. 2 — SEM images of $Ti_{10+x}V_{80-x}Fe_6Zr_4$ (x = 0~15) alloys. (a) x=0; (b) x=5; (c) x=10; (d) x=15.

[29] and 52Ti−12 V−36Cr alloy with additive of 2.2 wt% Zr [13], respectively. From practical application point of view, the activation of the hydrogen storage alloys under moderate conditions would be more desirable.

The maximum hydrogen absorption capacities of the studied alloys at 298 K are presented in Table 5. It can be seen that the electron/atom ratio of the alloys are all less than the critical value of 5.1 [5,11], bringing about relatively high absorption capacities of above 3 wt%. With the increase of x from 0 to 15, the maximum hydrogen absorption capacity of the alloy increases first and then decreases, which are 3.4 wt%, 3.5 wt%, 3.61 wt% and 3.18 wt%, respectively, indicating that the increase of Ti content can increase the hydrogen absorption capacity to a certain extent, however, the absorption capacity will reduce if the Ti content is too high. This phenomenon may be interpreted that the increase in the capacity is related to the expansion of the lattice whose effect is dominant over that of the reduction in V content as displayed in Fig. 4, in which the rise in lattice parameter is linear with the increase of Ti content from x = 0 to x = 10. However, the extent of increase in lattice parameter distinctly declines from x = 10 to x = 15, of which influence is dominated by the decrease in V content, possibly bringing about the reduction in the capacity.

Fig. 7 shows cyclic absorption curves of $Ti_{10+x}V_{80-x}Fe_6Zr_4$ (x = 0, 5, 10, 15) alloys at 298 K. It can be seen that hydrogen-absorbing rate of the 2nd to 5th cycles for all the alloys are enhanced compared with that of the 1st cycle (also shown in Fig. 6) and the saturated capacity is obtained within 3 min.

Yu et al. [29] reported that variation of hydrogen absorption rate of was attributed to difference in affinities of constituent elements with H in the first hydrogenation for Ti−xV−10Cr−(50−x)Mn (x = 20, 24, 28 and 32) alloys without exposure to air before activation and nearly no incubation time was observed, whereas the incubation times of 700−1600 s are observed for the alloys exposed to air before activation. However, the analysis on activation mechanism seems to be insufficient and cyclic absorption kinetics for these alloys was not addressed. Priyanka et al. [16] revealed that the higher hydrogenation rate of $Ti_{0.43}Zr_{0.07}Cr_{0.25}V_{0.25}$ in the initial stage could be attributed to the higher driving force due to large difference between the initial pressure and the equilibrium pressure at the beginning. However, the higher driving force mentioned above is an external test condition during the hydrogenation and the intrinsic absorption kinetics of the V-based alloys were not reported. Amol et al. [13] put forward that shorter incubation time meant giving faster intrinsic kinetics, the reason for which was also not mentioned. It should be noted that only the first hydrogenation was reported in these work. While in this study, the five cyclic absorption processes of the alloys have been investigated as displayed in Fig. 7.

It is interesting that nearly no incubation time of Ti−xV−10Cr−(50−x)Mn (x = 20, 24, 28 and 32) alloys was observed without exposure to air before activation, while distinct incubation period of 52Ti−12 V−36Cr with or without Zr addition was observed. Hence, in our opinion, for the V-based alloys with BCC and C14 Laves phases without exposure to air before activation, the incubation time should be controlled by the difficulty of formation of new cracks in the alloys, which is supposed to be associated with the C14 Laves phase because new cracks are more easily formed inside the C14 Laves phase at the initial stage of activation due to its higher brittleness than BCC phase [29,30].
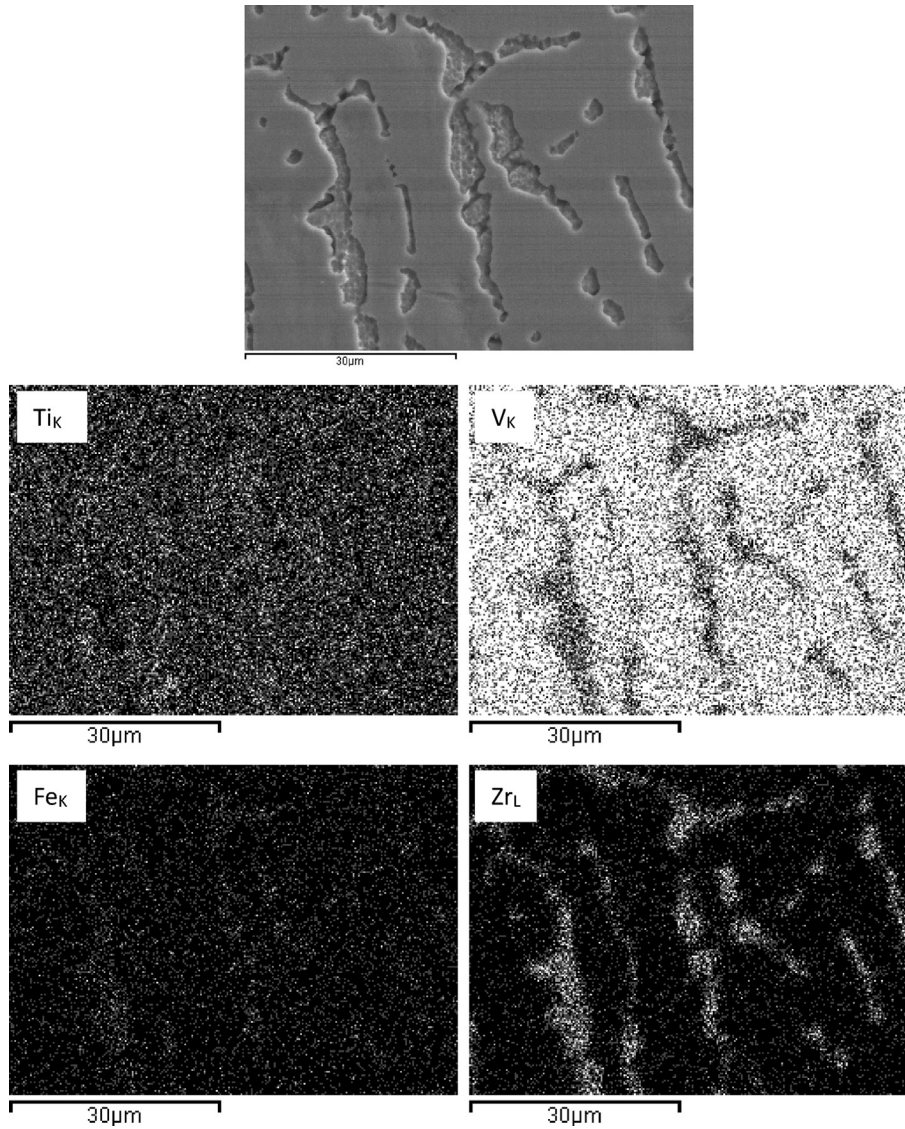
Fig. 3 – EDS mapping of $Ti_{15}V_{75}Fe_6Zr_4$ alloy.

Table 3 – EDS analysis results of each element of $Ti_{10+x}V_{80-x}Fe_6Zr_4$ (x = 0~15) alloys.

x	Phase	Composition(at%)			
		Ti	V	Fe	Zr
0	BCC	6.98	88.42	4	0.6
	C14	16.7	42.35	13.88	27.07
5	BCC	11.37	83.32	4.12	1.19
	C14	15.01	42.3	15.53	27.15
10	BCC	19.03	74.99	4.71	1.26
	C14	19.42	46.52	12.77	21.3
15	BCC	20.78	73.31	4.71	1.2
	C14	20.88	37.33	16.04	25.75

Fig. 4 – Functions of lattice parameter and average atomic radius of the BCC phase as x in $Ti_{10+x}V_{80-x}Fe_6Zr_4$ (x = 0~15) alloys.

From the viewpoint of practical application, the alloys in this study are exposed to air before activation. In this case, the incubation time of the alloys should be affected by the formation of oxide film on the alloy surface besides the factor of new cracks. During the activation process, once the chain
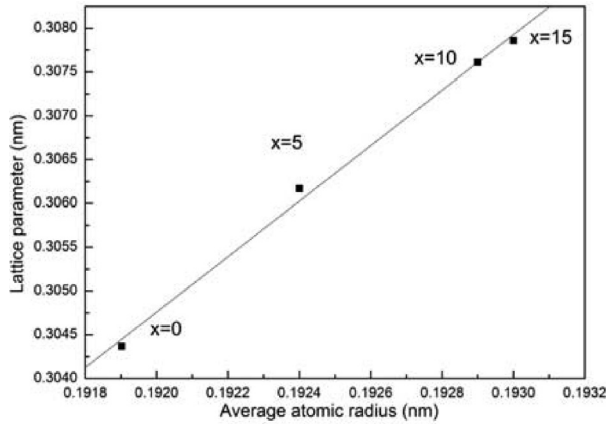
Fig. 5 – Relationship of lattice parameters and average atomic radius of the BCC phases in $Ti_{10+x}V_{80-x}Fe_6Zr_4$ ($x = 0$~15) alloys.
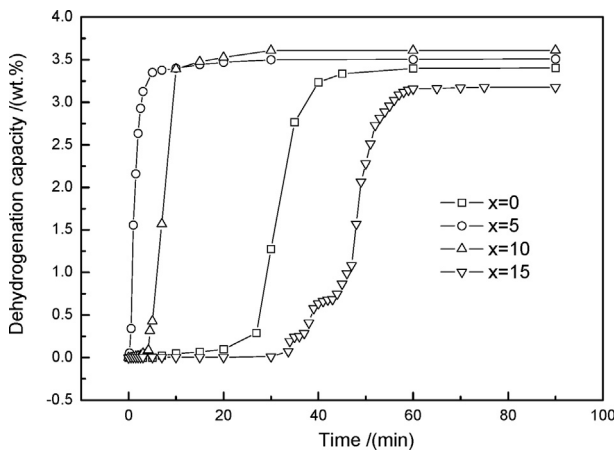
Fig. 6 – Activation hydriding curves of $Ti_{10+x}V_{80-x}Fe_6Zr_4$ ($x = 0$~15) alloys at 298 K.

Table 4 – The incubation time of $Ti_{10+x}V_{80-x}Fe_6Zr_4$ ($x = 0$, 5, 10, 15) alloys.

Ti content	$x = 0$	$x = 5$	$x = 10$	$x = 15$
Incubation time(s)	1620	12	249	2019

reaction of formation of new cracks launches, hydrogen-absorbing rate of the alloys will be high as shown in Fig. 6 and literature [13]. Furthermore, as displayed in Fig. 7, hydrogen-absorbing rate of the 2nd to 5th cycles for each alloy seems more rapid than that of the 1st cycle due to the existing

cracks after the 1st cycle. This further confirms the excellent intrinsic absorption kinetics of the BCC phase. On the other hand, compared with the 1st cycle, the hydrogenation of the 2nd to 5th cycles for each alloy is absent of incubation time, owing to the elimination of impact of oxide film on incubation time also caused by the existing cracks after the 1st cycle. This could well confirm the activation mechanism mentioned above for the oxidized alloys. In addition, the variation in hydrogen-absorbing rate of the 2nd to 5th cycles representing the intrinsic absorption kinetics of the BCC phase with increasing Ti content is not obvious, which indicates that the substitution of Ti for V would not change its good intrinsic absorption kinetics.

It is also revealed in Fig. 7 that the measured hydrogen absorption capacity reduces with cycling for all the alloys and the capacity attenuation rates are 93.5%, 87.1%, 87.0%, 87.2% at the 5th cycle for $x = 0$, 5, 10,15, respectively. It should be noted that BCC alloys have a large hydrogen solid solution range at low pressure [31], resulting in the existence of residual hydrogen in the hydrogenated samples even undergoing the evacuation for 30 min at 673 K. Thus, the attenuation of measured absorption capacity could not directly represent the hydrogen content change in the alloy [32].

Fig. 8 shows the desorption PCI curves of $Ti_{10+x}V_{80-x}Fe_6Zr_4$ ($x = 0-15$) samples at 353 K. The equilibrium plateau pressure (P_{eq}) is obtained from the midpoint of desorption isotherm plateau and the slope factor (S_f) is commonly expressed as:

$$S_f = \frac{d(\ln P)}{d(H/M)}$$

S_f reflects the steepness of the plateau.

The data of the PCI characteristics are summarized in Table 5. Here, the desorption capacity is defined as the amount of hydrogen desorbed when hydrogen pressure reduced from 3 to 0.001 MPa at 353 K.

With increasing x, the plateau pressure decreases drastically as displayed in Fig. 8. The plateau pressure is supposed to be related to cell volume of BCC and the distance between neighbouring hydrogen atoms [6,29]. Macroscopically, the expansion in cell volume of BCC phase in this study leads to a increase in volume of hydrogen absorbed in unit cell, theoretically bringing about a decrease in the decomposition pressure at a fixed hydrogen content and temperature according to ideal gas law. Additionally, the hydrogen desorption capacity increases first and then decreases, achieving the maximum at $x = 5$ and minimum at $x = 15$, corresponding to the similar change of the plateau width. Besides the plateau width, S_f is another important parameter to illuminate the plateau performance of hydrogen desorption. As seen in Table 5, S_f decreases first and then increases with increasing x,

Table 5 – The hydrogen storage characteristics of $Ti_{10+x}V_{80-x}Fe_6Zr_4$ ($x = 0$~15) alloys.

x	Electron-to-atom Ratio	Maximum hydrogen absorption capacity at 298 K/(wt.%)	Hydrogen desorption capacity (desorbed to 0.001 MPa) at 353 K/(wt.%)	Equilibrium plateau pressure P_{eq} at 353 K (MPa)	Slope factor (S_f)
0	5.04	3.40%	1.88%	0.511	2.57
5	4.99	3.50%	1.94%	0.170	1.81
10	4.94	3.61%	1.54%	0.040	2.75
15	4.89	3.18%	1.35%	0.012	4.16
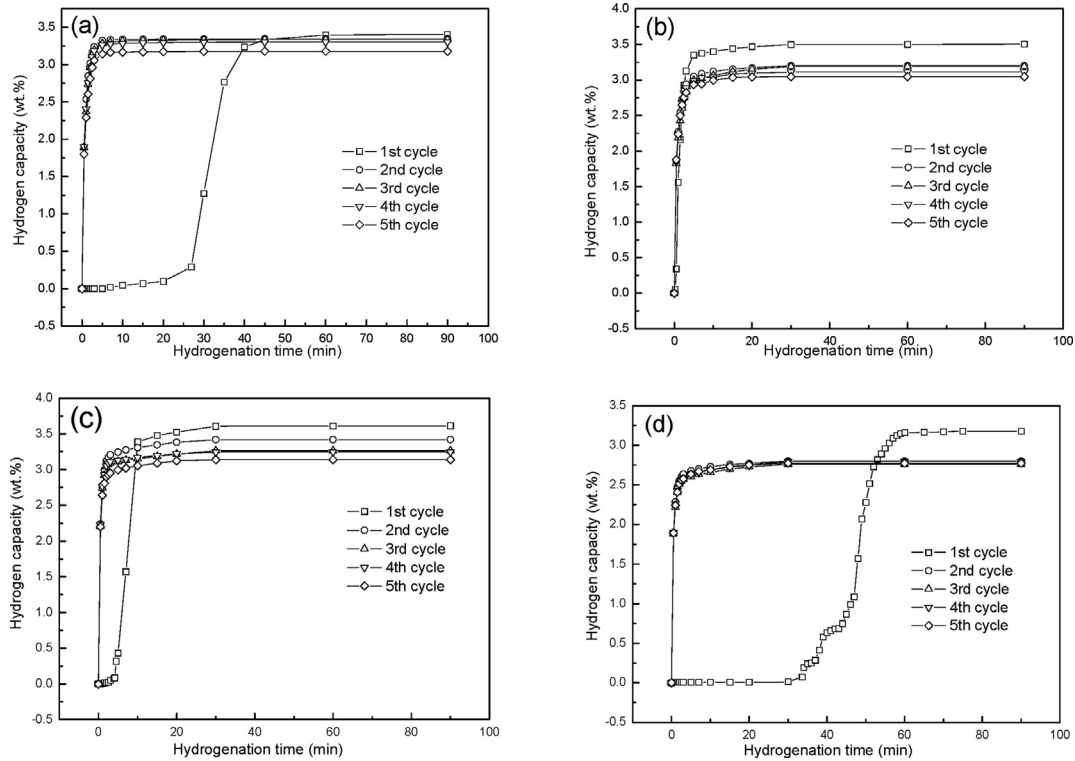
Fig. 7 – Cyclic absorption curves of $Ti_{10+x}V_{80-x}Fe_6Zr_4$ (x = 0~15) alloys at 298 K. (a) x = 0; (b) x = 5; (c) x = 10; (d) x = 15.
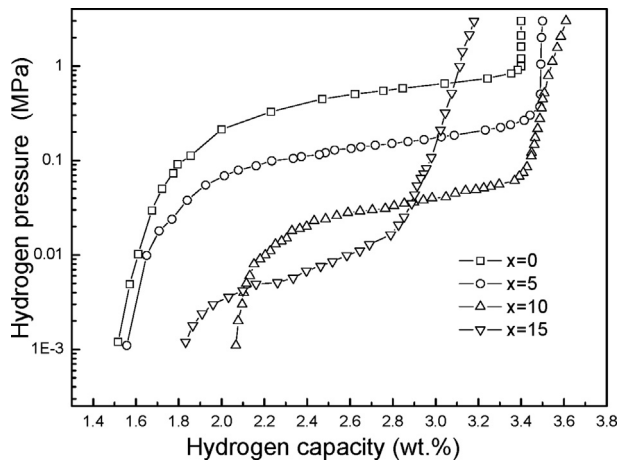
Fig. 8 – Desorption PCI curves of $Ti_{10+x}V_{80-x}Fe_6Zr_4$ (x = 0~15) samples at 353 K.
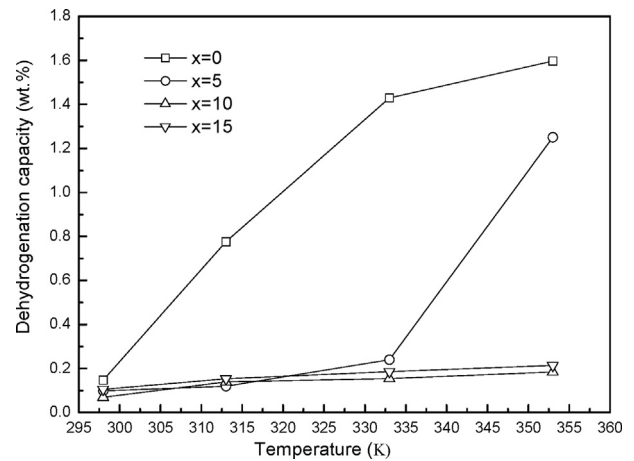
Fig. 9 – The hydrogen capacities of $Ti_{10+x}V_{80-x}Fe_6Zr_4$ (x = 0~15) samples desorbed to 0.1 MPa at different temperatures.

obtaining the minimum at x = 5 and maximum at x = 15, which may be resulted from the variation in strain energy of interstitial site in the alloys [29,33]. Combining S_f, plateau pressure and desorption capacity, it could be valuably found that the sample with x = 5 shows the best overall PCI performance.

From the point of view of practical application, the hydrogen capacities of the $Ti_{10+x}V_{80-x}Fe_6Zr_4$ (x = 0–15) samples desorbed to 0.1 MPa at different temperatures were measured and the results are shown in Fig. 9. The hydrogen desorption capacity of the sample with x = 0 increases significantly with the increase in temperature, from 0.15 wt%

at 298 K to 1.6 wt% at 353 K. In deep contrast, the desorption capacities of the samples with $x \geq 10$ remain low from 298 K to 333 K. Hence, it is necessary to investigate the phase structure and the state of hydrogen for dehydrided samples.

For comparison, XRD patterns of the hydrogenated samples at 298 K and those desorbed to 0.1 MPa at 333 K have been presented in Fig. 10. All the hydrogenated samples show the similarity in respect of XRD patterns (Fig. 10(a)), indicating the existence of VH_2-based FCC main phase and minor phases such as $VH_{0.81}$-based BCT phase, TiH-based phase and ZrH-based phase.
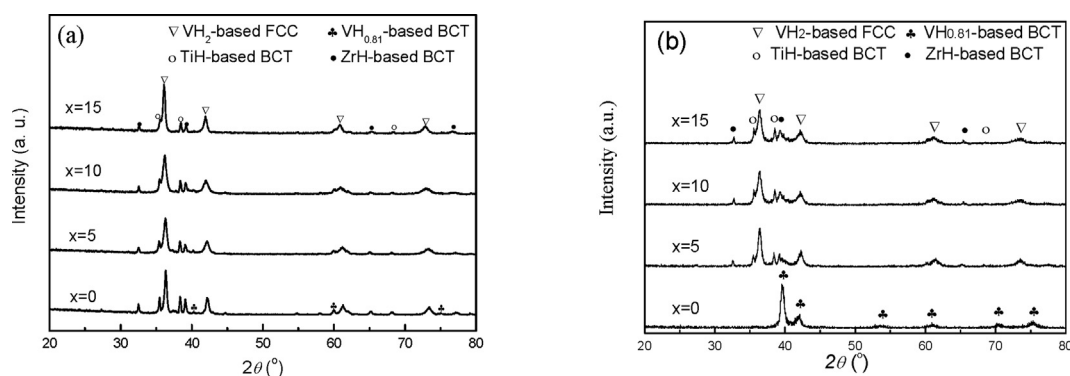
Fig. 10 — XRD patterns of $Ti_{10+x}V_{80-x}Fe_6Zr_4$ samples (a) hydrogenated at 298 K and (b) after dehydrogenation to 0.1 MPa at 333 K.

Table 6 — A comparison of the crystal characteristics of the main phase in $Ti_{10+x}V_{80-x}Fe_6Zr_4$ samples after hydrogenation at 298 K (defined as process A) and those desorbed to 0.1 MPa at 333 K (defined as process B).

Sample (x)	0		5		10		15	
Process	A	B	A	B	A	B	A	B
Main phase	FCC	BCT	FCC	FCC	FCC	FCC	FCC	FCC
Lattice parameter, a (nm)	0.42807	0.30288	0.42849	0.42649	0.42977	0.42661	0.43033	0.42677
Lattice parameter, c (nm)		0.34054						
Cell volume, V (nm^3)	0.07844	0.03124	0.07867	0.07758	0.07938	0.07764	0.07969	0.07773

For pure V metal, the deformed BCC solid solution phase containing hydrogen (α phase) is formed when absorbing a small amount of H, and the mono-hydride phase (β phase) with BCT structure and di-hydride phase (γ phase) with FCC structure are formed by further hydrogen absorption [34].

Hence, The appearance of VH_2-based FCC main phase (γ phase) is logical for the hydrogenated V-based samples in this study under high initial hydrogen pressure(4 MPa) [13,24]. However, the reason for the small amount coexistence of $VH_{0.81}$-based BCT phase (β phase) caused by the incomplete transition of β to γ phase needs further study. Obviously, the minor TiH-based and ZrH-based phases are attributed to the hydrogenation of the small amounts of Ti and Zr, while the majority of them may distribute in the main phase (γ phase).

As shown in Fig. 10(b), after dehydrogenation at 333 K, almost only $VH_{0.81}$-based hydride (β phase) with BCT structure is observed for the sample with $x = 0$, which indicates the relatively completed transition of γ to β phase, corresponding to the relatively high desorption capacity of 1.43 wt% shown in Fig. 9. It is also found in Fig. 9 that the desorption capacities of samples with $x \geq 5$ at 333 K seem to be so low that the XRD patterns (Fig. 10(b)) of dehydrided samples are almost unchanged, compared to those of the hydrogenated samples shown in Fig. 10(a). It is well known that the desorption capacity of the sample is closely related to the desorption equilibrium plateau pressure. While the desorption equilibrium plateau pressures of the samples with $x \geq 5$ appear to be such low even at 353 K (Fig. 8). The crystal characteristics of the main phase in $Ti_{10+x}V_{80-x}Fe_6Zr_4$ samples after hydrogenation at 298 K and dehydrogenation to 0.1 MPa at 333 K are determined by Rietveld refinement and the results are listed in Table 6. Compared with the hydrogenated samples, the cell volume of the main phase in the dehydrogenated samples drastically

reduces for $x = 0$, while slight reduction is observed for $x \geq 5$, which agrees well with Fig. 10.

Conclusions

$Ti_{10+x}V_{80-x}Fe_6Zr_4$ ($x = 0, 5, 10, 15$) hydrogen storage alloys are composed of BCC main phase and C14 Laves secondary phase that precipitates along the grain boundary of the former. With the increase of x, the lattice parameter of BCC phase in the alloy increases, which has a good linear relationship with its average atomic radius. All bulk alloys have relatively good activation behaviors and excellent hydriding kinetics. With increasing x, the incubation time of the alloy decreases first and then increases under the initial hydrogen pressure of 4 MPa at 298 K, obtaining the minimum value of 12 s at $x = 5$. Meanwhile, the maximum hydrogen absorption capacity of the alloy increases first and then decreases, achieving the maximum value of 3.61 wt% at $x = 10$. With the increase of x, the hydrogen desorption capacity of sample desorbed to 0.001 MPa at 353 K increases first and then decreases, reaching the maximum value of 1.94 wt% at $x = 5$, while that desorbed to 0.1 MPa at 353 K reduces, especially for $x = 10$ and 15, attaining the maximum value of 1.6 wt% at $x = 0$. After dehydrogenation to 0.1 MPa at 333 K, the main phase changes from γ to β phase for the sample with $x = 0$, while remains the same γ phase as that in the hydrogenated samples with $x \geq 5$.

Declaration of competing interest

The authors declare that they have no known competing financial interests or personal relationships that could have appeared to influence the work reported in this paper.

REFERENCES

[1] Zhou SJ, Zhang X, Wang L, Zhao YY, Xiong W, Li BQ, et al. Effect of element substitution and surface treatment on low temperature properties of $AB_{3.42}$-type La–Y–Ni based hydrogen storage alloy. Int J Hydrogen Energy 2021;46:3414–24.

[2] Zhang HW, Bao L, Chen YF, Fu L, Yuan YJ. Synergistic effects of La_2Mg_{17}/Ni/H system on hydrogen storage. Mater Lett 2021;291:129548.

[3] Liu HZ, Zhang LF, Ma HY, Lu CL, Luo H, Wang XH, et al. Aluminum hydride for solid-state hydrogen storage: structure, synthesis, thermodynamics, kinetics, and regeneration. J Energy Chem 2021;52:428–40.

[4] Akiba E, Iba H. Hydrogen absorption by Laves phase related BCC solid solution. Intermetallics 1998;6:461–70.

[5] Lynch JF, Maeland AJ, Libowitz GG. Lattice parameter variation and thermodynamics of dihydride formation in the vanadium-rich V–Ti–Fe/H_2 system. Z Phys Chem 1985;145:51–9.

[6] Abdul JM, Chown LH. Influence of Fe on hydrogen storage properties of V-rich ternary alloys. Int J Hydrogen Energy 2016;41:2781–7.

[7] Challet S, Latroche M, Heurtaux F. Hydrogenation properties and crystal structure of the single BCC $(Ti_{0.355}V_{0.645})_{100-x}M_x$ alloys with M=Mn, Fe, Co, Ni (x=7, 14 and 21). J Alloys Compd 2007;439:294–301.

[8] Chen XY, Chen RR, Ding X, Fang HZ, Li XZ, Ding HS, et al. Effect of phase formation on hydrogen storage properties in Ti-V-Mn alloys by zirconium substitution. Energy 2019;166:587–97.

[9] Dixit V, Huot J. Structural, microstructural and hydrogenation characteristics of Ti-V-Cr alloy with Zr-Ni addition. J Alloys Compd 2019;776:614–9.

[10] Hang ZM, Chen LX, Xiao XZ, Li SQ, Chen CP, Lei YQ, et al. The effect of Cr content on the structural and hydrogen storage characteristics of $Ti_{10}V_{80-x}Fe_6Zr_4Cr_x$ (x=0–14) alloys. J Alloys Compd 2010;493:396–400.

[11] Hang ZM, Xiao XZ, Tan DZ, He ZH, Li WP, Li SQ, et al. Microstructure and hydrogen storage properties of $Ti_{10}V_{84-x}Fe_6Zr_x$ (x=1–8) alloys. Int J Hydrogen Energy 2010;35:3080–6.

[12] Kadono J, Maruoka T, Nakazawa D, Hoshiyama Y, Miyake H. Measuring the effects of boron mass addition to V–Fe hydrogen storage alloys on their hydrogen absorbing–desorbing characteristics and loss of boron by hydrogenation by employing new analysis methods; hybrid of Sieverts' method, inert gas fusion method, and gravimetric method. Int J Hydrogen Energy 2017;42:996–1003.

[13] Kamble A, Sharma P, Huot J. Effect of addition of Zr, Ni, and Zr-Ni alloy on the hydrogen absorption of Body Centred Cubic 52Ti-12V-36Cr alloy. Int J Hydrogen Energy 2018;43:7424–9.

[14] Luo L, Li YZ, Zhai TT, Hu F, Zhao ZW, Bian X, et al. Microstructure and hydrogen storage properties of $V_{48}Fe_{12}Ti_{15-x}Cr_{25}Al_x$ (x=0, 1) alloys. Int J Hydrogen Energy 2019;44:25188–98.

[15] Mao Y, Yang S, Wu CL, Luo LS, Chen YG. Preparation of $(FeV80)_{48}Ti_{26+x}Cr_{26}$($x$=0–4) alloys by the hydride sintering method and their hydrogen storage performance. J Alloys Compd 2017;705:533–8.

[16] Ruz P, Banerjee S, Halder R, Kumar A, Sudarsan V. Thermodynamics, kinetics and microstructural evolution of $Ti_{0.43}Zr_{0.07}Cr_{0.25}V_{0.25}$ alloy upon hydrogenation. Int J Hydrogen Energy 2017;42:11482–92.

[17] Wang Q, Dai X, Wu CL, Mao Y, Chen YG, Cao XZ, et al. Lattice defects and micro-strains in $V_{60}Ti_{25}Cr_3Fe_{12}$ alloy and influence on the ab/desorption of hydrogen. J Alloys Compd 2020;830:154675.

[18] Wu CL, Wang Q, Mao Y, Huang LW, Chen YG, Dai X. Relationship between lattice defects and phase transformation in hydrogenation/dehydrogenation process of the $V_{60}Ti_{25}Cr_3Fe_{12}$ alloy. Int J Hydrogen Energy 2019;44:9368–77.

[19] Zadorozhnyy V, Sarac B, Berdonosova E, Karazehir T, Lassnig A, Gammer C, et al. Evaluation of hydrogen storage performance of ZrTiVNiCrFe in electrochemical and gas-solid reactions. Int J Hydrogen Energy 2020;45:5347–55.

[20] Balcerzak M, Wagstaffe M, Robles R, Pruneda M, Noei H. Effect of Cr on the hydrogen storage and electronic properties of BCC alloys: experimental and first-principles study. Int J Hydrogen Energy 2020;45:28996–9008.

[21] Yu XB, Feng SL, Wu Z, Xia BJ, Xu NX. Hydrogen storage performance of Ti–V-based BCC phase alloys with various Fe content. J Alloys Compd 2005;393:128–34.

[22] Zhu YF, Liu YF, Hua F, Li LQ. Effect of rapid solidification on the structural and electrochemical properties of the Ti–V-based hydrogen storage electrode alloy. J Alloys Compd 2008;463:528–32.

[23] Yan YG, Chen YG, Liang H, Zhou XX, Wu CL, Tao MD, et al. Hydrogen storage properties of V–Ti–Cr–Fe alloys. J Alloys Compd 2008;454:427–31.

[24] Dixit V, Huot J. Investigation of the microstructure, crystal structure and hydrogenation kinetics of Ti-V-Cr alloy with Zr addition. J Alloys Compd 2019;785:1115–20.

[25] Tsukahara M, Takahashi K, Mishima T, Isomura A, Sakai T. Influence of various additives in vanadium-based alloys $V_3TiNi_{0.56}$ on secondary phase formation, hydrogen storage properties and electrode properties. J Alloys Compd 1996;245:59–65.

[26] Kuriiwa T, Tamura T, Amemiya T, Fuda T, Kamegawa A, Takamura H, et al. New V-based alloys with high protium absorption and desorption capacity. J Alloys Compd 1999;293–295:433–6.

[27] Liang H, Chen YG, Yan YG, Wu CL, Tao MD. Cyclic properties of hydrogen absorption and desorption in V–Ti–Cr–Fe(Al,Si) alloy. Mater Sci Eng, A 2007;448:128–34.

[28] Yu XB, Wu Z, Xia BJ, Xu NX. Hydrogen storage performance of quenched Ti–V-based alloy. J Alloys Compd 2004;373:134–6.

[29] Yu XB, Wu Z, Xia BJ, Xu NX. Enhancement of hydrogen storage capacity of Ti–V–Cr–Mn BCC phase alloys. J Alloys Compd 2004;372:272–7.

[30] Mouri T, Iba H. Hydrogen-absorbing alloys with a large capacity for a new energy carrier. Mater Sci Eng, A 2002;329–331:346–50.

[31] Kabutomori T, Takeda H, Wakisaka Y, Ohnishi K. Hydrogen absorption properties of Ti–Cr–A (A ≡ V, Mo or other transition metal) B.C.C. solid solution alloys. J Alloys Compd 1995;231:528–32.

[32] Itoh H, Arashima H, Kubo K, Kabutomori T, Ohnishi K. Improvement of cyclic durability of BCC structured Ti–Cr–V alloys. J Alloys Compd 2005;404–406:417–20.

[33] Seo C-Y, Kim J-H, Lee PS, Lee J-Y. Hydrogen storage properties of vanadium-based b.c.c. solid solution metal hydrides. J Alloys Compd 2003;348:252–7.

[34] Kumar S, Balasubramaniam R. Theoretical analysis of hysteresis during hydrogen transformations in the vanadium-hydrogen system. Int J Hydrogen Energy 1995;20:211–20.

基本信息				☆ 登录收藏

期刊名字　Processes
PROCESSES

LetPub评分

5.9　★★☆☆☆　77人评分　**我要评分** ✏

声誉	5.0
影响力	5.7
速度	9.4

微信扫码收藏此期刊

期刊ISSN	2227-9717
2021-2022最新影响因子 （数据来源于搜索引擎）	注册或登录后，查看影响因子和历年趋势图
2021-2022自引率	13.20%　注册或登录后，查看自引率趋势图
h-index ⓘ	2

CiteScore ⓘ

CiteScore	SJR	SNIP	CiteScore排名			
			学科	分区	排名	百分位
3.50	0.474	0.889	大类：Chemical Engineering 小类：Chemical Engineering (miscellaneous)	Q2	19 / 42	55%
			大类：Chemical Engineering 小类：Process Chemistry and Technology	Q3	34 / 61	45%
			大类：Chemical Engineering 小类：Bioengineering	Q3	96 / 151	36%

期刊简介	Processes (ISSN 2227-9717) provides an advanced forum for process related research in chemistry, biology and allied engineering fields. The journal publishes regular research papers, communications, letters, short notes and reviews. Our aim is to encourage researchers to publish their experimental, theoretical and computational results in as much detail as necessary. There is no restriction on paper length or number of figures and tables.
期刊官方网站	https://www.mdpi.com/journal/processes
期刊投稿网址	https://login.mdpi.com/login?_target_path=https%3A%2F%2Fsusy.mdpi.com%2Fuser%2Flogin%3FauthAll%3Dtrue
是否OA开放访问	Yes
OA期刊相关信息 OPEN ACCESS	**文章处理费：** 需要（CHF2000;） **文章处理费豁免：** 没有 **其他费用：** 没有 **期刊主题关键词：** process engineering、chemical reactions、process design **相关链接：** Aims & Scope　Author Instructions　Editorial Board　Blind peer review
通讯方式	ST ALBAN-ANLAGE 66, BASEL, SWITZERLAND, CH-4052
出版商	MDPI (Basel, Switzerland)
涉及的研究方向	Chemical Engineering-Bioengineering
出版国家或地区	Switzerland
出版语言	English
出版周期	
出版年份	2013
年文章数 ⓘ	2198　注册或登录后，查看年文章数趋势图
Gold OA文章占比	95.00%
研究类文章占比： 文章÷（文章＋综述）	89.35%

WOS期刊SCI分区 ⓘ （**2021-2022年最新版**）	WOS分区等级：2区

按学科分区	
ENGINEERING, CHEMICAL	Q2

中科院《国际期刊预警 **名单（试行）》名单** ⓘ	2021年12月发布的2021版：不在预警名单中 2021年01月发布的2020版：预警等级：低

中科院SCI期刊分区
（**2021年12月最新基础版**）

注册或登录后，查看中科院SCI期刊分区趋势图

大类学科		小类学科		Top期刊	综述期刊
工程技术	3区	ENGINEERING, CHEMICAL 工程：化工	4区	否	否

中科院SCI期刊分区
（**2021年12月最新升级版**）ⓘ

大类学科		小类学科		Top期刊	综述期刊
工程技术	4区	ENGINEERING, CHEMICAL 工程：化工	3区	否	否

中科院SCI期刊分区
（**2020年12月旧的升级版**）

大类学科		小类学科		Top期刊	综述期刊
工程技术	3区	ENGINEERING, CHEMICAL 工程：化工	3区	否	否

Article

Enhancing Hydrogen Storage Kinetics and Cycling Properties of NaMgH₃ by 2D Transition Metal Carbide MXene Ti₃C₂

Zhouming Hang [1,2,3], Zhencan Hu [4], Xuezhang Xiao [4,*], Ruicheng Jiang [4] and Meng Zhang [4]

[1] College of Mechanical and Automotive Engineering, Zhejiang University of Water Resources and Electric Power, Hangzhou 310018, China; hangzhm@zjweu.edu.cn
[2] Zhejiang Engineering Research Center for Advanced Hydraulic Equipment, Zhejiang University of Water Resources and Electric Power, Hangzhou 310018, China
[3] Key Laboratory for Technology in Rural Water Management of Zhejiang Province, Zhejiang University of Water Resources and Electric Power, Hangzhou 310018, China
[4] State Key Laboratory of Silicon Materials and School of Materials Science and Engineering, Zhejiang University, Hangzhou 310027, China; 21726113@zju.edu.cn (Z.H.); 21726011@zju.edu.cn (R.J.); 11726062@zju.edu.cn (M.Z.)
[*] Correspondence: xzxiao@zju.edu.cn

Abstract: Metal hydrides have recently been proposed for not only hydrogen storage materials but also high-efficiency thermal storage materials. NaMgH₃ contains a considerable theoretical thermal storage density of 2881 kJ/kg. However, its sluggish de/re-hydrogenation reaction kinetics and poor cycling stability exhibit unavailable energy efficiency. Doping with active catalyst into NaMgH₃ is deemed to be a potential strategy to mitigate these disadvantages. In this work, the enhancement of de/re-hydrogenation kinetics and cycling properties of NaMgH₃ is investigated by doping with lamellar-structure 2D carbon-based MXene, Ti₃C₂. Results shows that introducing 7 wt.% Ti₃C₂ is proved to perform excellent catalytic efficiency for NaMgH₃, dramatically reducing the two-step hydrogen desorption peak temperatures (324.8 and 345.3 °C) and enhancing the de/re-hydrogenation kinetic properties with the hydrogen desorption capacity of 4.8 wt.% H_2 within 15 min at 365 °C and absorption capacity of 3.5 wt.% H_2 within 6 s. Further microstructure analyses reveal that the unique lamellar-structure of Ti₃C₂ can separate the agglomerated NaMgH₃ particles homogeneously and decrease the energy barriers of two-step reaction of NaMgH₃ (114.08 and 139.40 kJ/mol). Especially, lamellar-structure Ti₃C₂ can improve the reversibility of hydrogen storage of NaMgH₃, rendering 4.6 wt.% H_2 capacity remained after five cycles. The thermal storage density of the composite is determined to be 2562 kJ/kg through DSC profiles, which is suitable for thermal energy storage application.

Keywords: hydrogen storage materials; NaMgH₃; MXene; lamellar-structure; cycling performances

1. Introduction

Sodium-based hydrides such as NaH, MgH₂ (simple binary hydrides), NaBH₄ (borohydride), NaAlH₄ (alanates hydride), and NaMgH₃ (perovskite hydride) have been researched as promising candidates for hydrogen storage or thermal energy storage during the past decades [1–8]. As the GdFeO₃-type perovskite (space group *Pnma*) hydride, NaMgH₃ has received considerable attention for its high gravimetric and volumetric hydrogen densities (6 wt.% and 88 kg/m³) and possesses a considerable theoretical thermal storage gravimetric density (2881 kJ/kg) with reversible two-step de/re-hydrogenation process: [9–15]

$$NaMgH_3 \rightarrow NaH + Mg + H_2 \qquad (1)$$

$$NaH + Mg \rightarrow Na + Mg + 1/2\ H_2 \qquad (2)$$
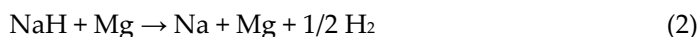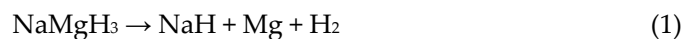
Especially, $NaMgH_3$ is considered as a potential thermal energy medium for concentration solar power (CSP) because of the high thermodynamic stability [16]. In particular, as a suitable candidate for thermal energy storage (TES), $NaMgH_3$ has several obvious advantages: high hydrogen storage capacity, low and flat hydrogen de/absorption pressure and plateau, negligible hysteresis, high thermal storage density, and low cost of raw materials [7]. In addition, de/re-hydrogenation kinetics performance and cycling properties are also important parameters to determine whether it is available to TES. However, the further applications to thermal energy storage are limited by sluggish de/re-hydrogenation kinetic performance and pronounced degradation of cycling properties of $NaMgH_3$.

Much attention has been focused on improving de/re-hydrogenation kinetics performance and cycling properties of $NaMgH_3$ during the last few decades [17–21]. It has been proved that adding Li or K into $NaMgH_3$ would make Li or K partially take the place of the Na position and the formation of distorted perovskite structure would enhance the de-hydrogenation kinetics performance [17,18]. Li et al. [19] improved the cycling properties through in situ embedding of Mg_2NiH_4 and YH_3 nanoparticles in $NaMgH_3$. Except alkali metal and metal hydrides, the Ti-based catalysts have been found to possess remarkably high catalytic activity. Wang's group [20] decreased the onset desorption temperature of $NaMgH_3$ to 328 K with 153.47 kJ/mol by introduced K_2TiF_6 as a dopant. Moreover, it was confirmed that TiF_3 can significantly reduce the activation energy of $NaMgH_3$ to 104 kJ/mol [18].

As a new type of two-dimension materials, MXenes have been successfully synthesized through etching ternary carbides, nitrides, or carbonitrides (MAX) with HF or in situ HF [22–25]. The general formula of MXenes is $M_{n+1}X_nT_x$ (n = 1–3), where M represents a transition metal, X is carbon and/or nitrogen, and T_x stands for the surface terminations [26]. The carbide transition metal MXene, such as Ti_3C_2, possesses a particularly lamellar structure, showing promising application as an anode material for Li-ion batteries [27,28]. Furthermore, much effort has been devoted to exploring the superior catalytic effect of Ti_3C_2 on de/re-hydrogenation reactions of hydrides [29–34]. Liu et al. [29,30] observed a strong catalytic effect of Ti_3C_2 in de/re-hydrogenation kinetics properties on both MgH_2 and $NaAlH_4$. In particular, Ti_3C_2 tremendously improved the cycling stability of $NaAlH_4$, with the de/re-hydrogenation performance remaining nearly constant over 10 cycles. The superior catalytic efficiency of Ti_3C_2 has also been proven on $LiNa_2AlH_6$ and $Li_{1.3}Na_{1.7}AlH_6$ [31,32]. Therefore, the superior catalytic efficiency of the lamellar-structure Ti_3C_2 is highly anticipated to expand to the $NaMgH_3$.

There are indeed many other higher hydrogen storage capacity compounds, such as $LiBH_4$ with 18.5 wt.%, MgH_2 with 7.6 wt.% and $NaAlH_4$ with 5.6 wt.% [35,36]. Although the reversible hydrogen storage capacity of $NaMgH_3$ is about 6 wt.%, it exhibits other engineering feasibility in heat storage, accompanying the reversible hydrogen storage process [37]. From pressure–composition isotherm (PCI) measurements, the enthalpy, ΔH(des), and entropy, ΔS(des), of desorption for Equation (1) were determined as 86.6 $kJ\cdot mol^{-1}\ H_2$ and 132.2 $J\cdot mol^{-1}\cdot H_2\cdot K^{-1}$. The enthalpy and entropy of desorption for Equation (2) correspond to those for pure NaH (ΔH(des) = 116 $kJ\cdot mol^{-1}\cdot H_2$ and ΔS(des) = 168.2 $J\cdot mol^{-1}\cdot H_2\cdot K^{-1}$). The theoretical gravimetric heat storage capacity of Equations (1) and (2) is 2881 $kJ\cdot kg^{-1}$ (Equation (1) = 1721 $kJ\cdot kg^{-1}$, Equation (2) = 1160 $kJ\cdot kg^{-1}$). Therefore, $NaMgH_3$ would be an ideal thermal storage medium during the hydrogen storage process. However, further applications for thermal energy storage are limited by sluggish de/re-hydrogenation kinetic performance and pronounced degradation of $NaMgH_3$ cycling properties.

In this work, the 2D MXenes Ti_3C_2 with a unique lamellar-structure was introduced into $NaMgH_3$ for enhancing its de/re-hydrogenation kinetics and cycling behaviors for the first time. Five composites including $NaMgH_3$-x wt.% Ti_3C_2 (x = 0, 3, 5, 7, and 9) were synthesized via ball-milling. Among them, the 7 wt.% Ti_3C_2-containing $NaMgH_3$ shows the optimal de/re-hydrogenation storage performance as it can desorb 4.8 wt.% H_2 in 15 min at 365 °C and then can be easily hydrogenated at 300 °C under 80 bar H_2. More importantly, the reversible hydrogen storage performance stays at a relatively high level after 5 cycles. It is confirmed that the 2D Ti_3C_2 can disperse the agglomerated $NaMgH_3$ particles homogeneously, decrease the activation energy of $NaMgH_3$, and prevent Na from separating Mg during the cycles. Moreover, the thermal storage density for $NaMgH_3$-7 wt.% Ti_3C_2 is evaluated to be 2562 kJ/kg through DSC profile.

2. Materials and Methods

The lamellar-structure Ti_3C_2 was prepared via etching the Ti_3AlC_2 (98% purity, Laizhou Kai Xi Ceramic Materials Co., Ltd., Laizhou, China) with the HF, which was mixed by combining 15 mL HCl (12 M), 15 mL deionized water and 1.98 g LiF. Then 3 g Ti_3AlC_2 precursor was immersed into the in situ HF and transferred to a 100 mL Teflon-lined autoclave. The Ti_3AlC_2 was treated with a 48-hour heat treatment in an oil bath at 60 °C. After heat treatment, the precursor was washed with deionized water through centrifugation treatment. The final pH of this precursor should reach 6 and then further drying could be carried out. The drying process was operated at 80 °C for 24 h under vacuum.

The as-formed lamellar-structure Ti_3C_2 was doped into $NaMgH_3$ as a catalyst to enhance de/re-hydrogenation kinetics and cycling properties. Five composites of $NaMgH_3$-x wt.% Ti_3C_2 (x = 0, 3, 5, 7, and 9) were synthesized by milling with stainless steel balls of which the weight ratio to composites was 40:1 under 10 bar H_2 for 12 h at 400 rpm using a planetary ball mill (QM-3SP4, Nanjing, China).

The phase transformations, structures and morphological features of Ti_3C_2 and $NaMgH_3$-x wt.% Ti_3C_2 (x = 0, 3, 5, 7, and 9) composites were characterized via X-ray diffraction (XRD, PANalytical, The Netherlands, Cu Kα) and scanning electron microscopy (SEM, Hitachi FSEM, SU-70, Tokyo, Japan). During the XRD and SEM analyses, all samples were protected by a laboratory-made container filled with argon for preventing samples from reacting with oxygen and water. Additionally, the de/re-hydrogenation performance of $NaMgH_3$-x wt.% Ti_3C_2 (x = 0, 3, 5, 7, and 9) composites were examined by a homemade Sieverts-type apparatus. The temperature-programmed desorption (TPD) analyses were tested with the heating rate of 5 °C/min from 25 to 450 °C under vacuum. The hydrogen desorption kinetics of all composites were examined at 365 and 350 °C with a base pressure of 3×10^{-2} bar H_2. The hydrogen absorption kinetics were examined at 400, 350, and 300 °C under 80 bar H_2 for 1 h. The cycling property tests were determined by a repeated de/re-hydrogenation procedure at 400 °C, but changing the back pressure from 3×10^{-2} to 60 bar H_2. The gravimetric heat storage capacity and heat change of composites were determined using a differential scanning calorimeter (DSC).

3. Results and Discussion

First, the successful synthesis of lamellar-structure MXene Ti_3C_2 was confirmed through XRD and SEM analyses (Figure 1). It is obvious that the strongest and sharpest XRD diffraction peaks of Ti_3AlC_2 at $2\theta = 39°$ totally disappeared after etching treatment, which were replaced by another curve, the XRD pattern of Ti_3C_2. The diffraction peaks of as-formed Ti_3C_2 belonging to (002) and (004) are significantly broadened and shift to lower angles. Especially, the diffraction (002) peak was much stronger than before. Furthermore, the insert SEM image obviously suggests that the as-formed Ti_3C_2 exhibited a 2D lamellar-structure morphology, which was etched by in situ HF treatment and effectively separated by LiF [22].
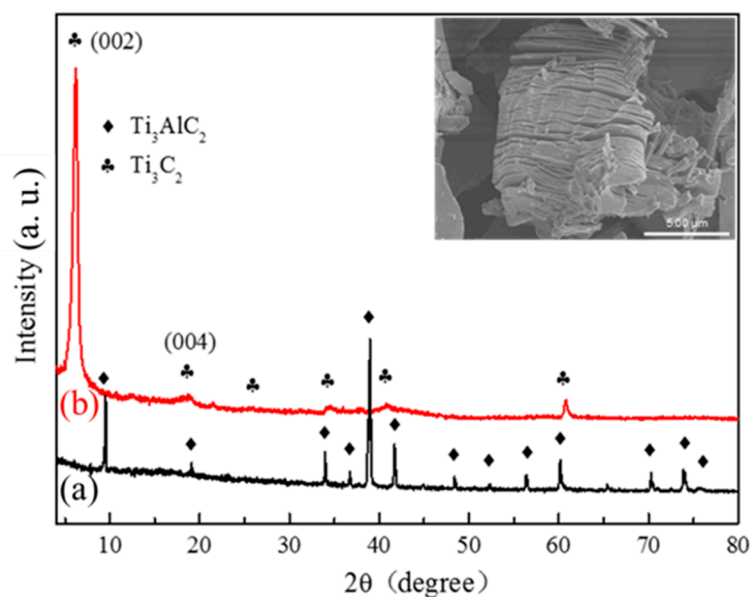
Figure 1. XRD patterns of (**a**) Ti₃AlC₂ and (**b**) as-prepared Ti₃C₂. The insert is the SEM image of Ti₃C₂.

Five composites of $NaMgH_3$-x wt.% Ti_3C_2 (x = 0, 3, 5, 7, and 9) were formed/synthesized by doping the as-prepared Ti_3C_2 into $NaMgH_3$ by ball milling, and the phase components and structures were determined by XRD, as displayed in Figure 2. As can be seen from the XRD analyses, only $NaMgH_3$ and MgO can be obviously identified in all five composites. The appearance of MgO phase is due to the impurity of Mg powders during the synthesis of pure $NaMgH_3$. It is almost impossible to find the diffraction peaks belonging to lamellar-structure Ti_3C_2 in these five patterns due to the small amounts of Ti_3C_2 additive [34]. The other possibility is that the ball milling destroyed the multilayered structure of Ti_3C_2. Therefore, the XRD results indicate the successful synthesis of the five composites without any other impurity peaks.
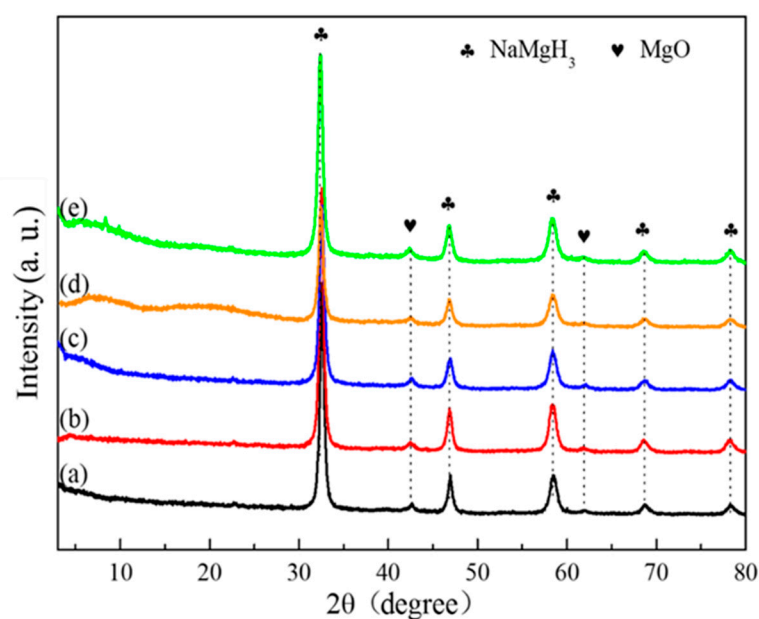
Figure 2. XRD patterns of (**a**) pure $NaMgH_3$, (**b**) $NaMgH_3$-3 wt.% Ti_3C_2, (**c**) $NaMgH_3$-5 wt.% Ti_3C_2, (**d**) $NaMgH_3$-7 wt.% Ti_3C_2, and (**e**) $NaMgH_3$-9 wt.% Ti_3C_2.

After assessing the phase components and morphology of $NaMgH_3$-x wt.% Ti_3C_2 (x = 0, 3, 5, 7, and 9) samples, the hydrogen desorption kinetics of all samples were evaluated

by DSC, TPD, and isothermal dehydrogenation measurements (Figure 3). As expected, doping a certain amount of Ti_3C_2 remarkably decreases the hydrogen desorption temperature in contrast to pure $NaMgH_3$ (Figure 3a). The first- and second-step dehydrogenation temperatures of $NaMgH_3$-3 wt.% Ti_3C_2 decreased from 372.3 and 380.3 °C to 344.5 and 358.4 °C, exhibiting 27.8 and 21.9 °C reduction, respectively. With increasing the Ti_3C_2 content to 5, 7, or 9 wt.%, the first-step dehydrogenation temperatures are further reduced to 327.5, 324.8 and 320.3 °C, respectively. Meanwhile, the second-step dehydrogenation temperatures of these samples declined to 341.3, 345.3, and 341.8 °C, respectively.
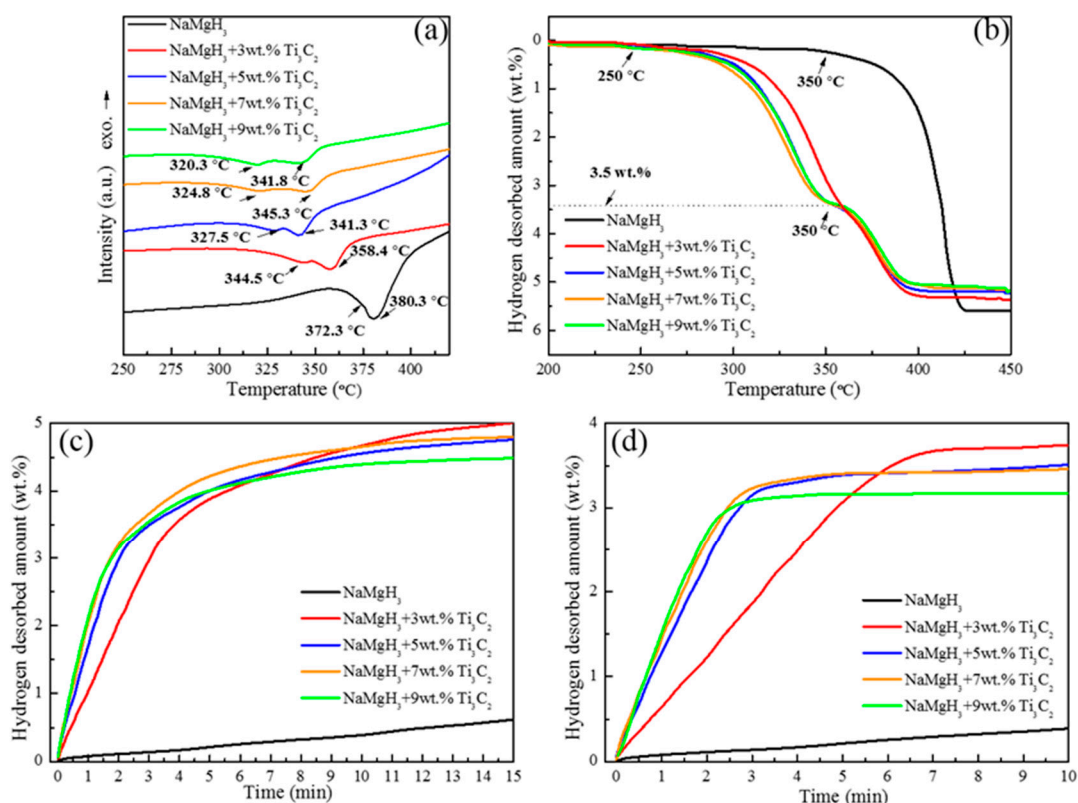
Figure 3. (**a**) DSC, (**b**) TPD, and isothermal dehydrogenation curves at (**c**) 365 °C and (**d**) 350 °C for $NaMgH_3$-x wt.% Ti_3C_2 (x = 0, 3, 5, 7, and 9) samples.

Combined with the TPD results (Figure 3b), more hydrogen desorption kinetic properties of $NaMgH_3$ undoped/doped with Ti_3C_2 are revealed. First, doping with 3 wt.% Ti_3C_2 reduces the onset dehydrogenation temperature of pure $NaMgH_3$ tremendously, from 350 °C to 250 °C. In particular, further increasing the content of Ti_3C_2 to 5, 7, or 9 wt.% allows around 3.5 wt.% H_2 to release (first-step decomposition reaction) below 350 °C. Importantly, the Ti_3C_2 sample containing 7 wt.% performs faster dehydrogenation kinetics than that of others below 350 °C. Nevertheless, the dehydrogenation capacity suffers a small loss, from 5.6 wt.% H_2 to 5.4, 5.3, 5.2, and 5.1 wt.% H_2, for the $NaMgH_3$-x wt.% Ti_3C_2 (x = 3, 5, 7, and 9) samples, respectively, which is mainly due to the dead weight of Ti_3C_2 and existence of MgO.

More specific dehydriding kinetic characterizations were carried out through the isothermal dehydrogenation measurements at 365 and 350 °C (Figure 3c,d). Just as shown by the earlier research, the sample containing 7 wt.% Ti_3C_2 exhibits the best dehydriding kinetic properties at 365 and 350 °C, desorbing 4.8 wt.% H_2 in 15 min and 3.4 wt.% H_2 in 5 min, respectively. However, for the pure $NaMgH_3$, only 0.6 wt.% H_2 is released in 15 min at 365 °C. As the temperature decreases to 350 °C, the pure $NaMgH_3$ sample only desorbs 0.2 wt.% H_2 in 5 min.

As a result, it is obvious that doping of 7 wt.% Ti₃C₂ leads to a tremendous improvement in the dehydriding kinetic properties of NaMgH₃. Furthermore, considering the observed results, including the dehydrogenation temperatures, dehydrogenation kinetic performance, and dehydrogenation capacities, the NaMgH₃-7 wt.% Ti₃C₂ composite exhibits the best energy efficiency and represents the optimal constituent.

To further understand the reason for such a huge dehydrogenation property gap between NaMgH₃-7 wt.% Ti₃C₂ and pure NaMgH₃, the DSC analyses were measured at different heating rates (1, 2, 5, and 8 °C/min) (Figure 4a,b). The activation energy (E_a) corresponding to the two-step dehydrogenation reactions of both two composites are quantitatively shown in Figure 4c and Table 1, determined by Kissinger fitting methods [38] (Equation (3)).

$$\ln(\beta/T_p^2) = -E_a/RT_p + \ln(AR/E_a) \tag{3}$$

$$\ln(\beta/T_p^2) = -E_a/RT_p + \ln(AR/E_a) \tag{4}$$

where β is the heating rate, T_p represents peak temperature, A is the pre-exponential factor, and R represents the gas constant.
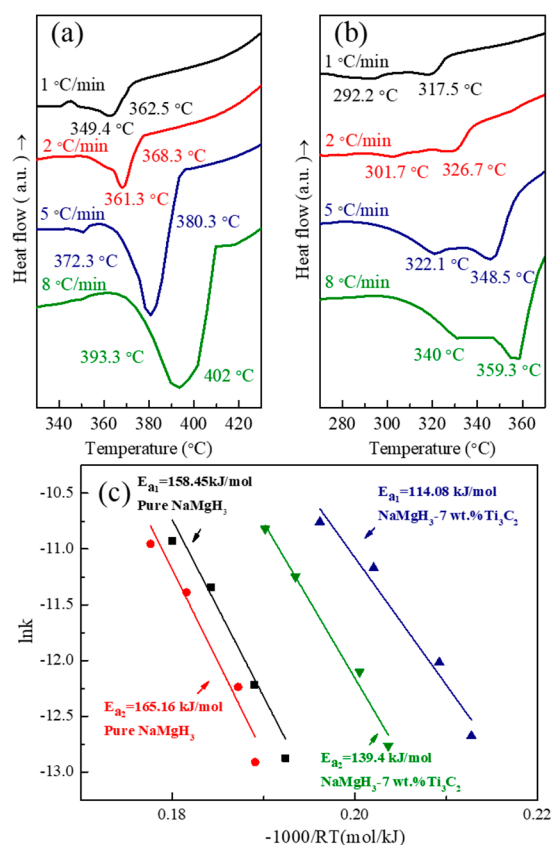
Figure 4. DSC curves for (**a**) pure NaMgH₃; (**b**) NaMgH₃-7 wt.% Ti₃C₂ at different heating rates; and Kissinger plots of (**c**) first- and second-step dehydrogenation of both samples.

Table 1. Activation energies (E_a) for the dehydrogenation of the NaMgH₃ sample undoped and doped with 7 wt.% Ti₃C₂.

Dopant	Apparent Activation Energy E_a (kJ/mol)	
	NaMgH₃ (First-Step)	NaMgH₃ (Second-Step)
Undoped	158.45	165.16
7 wt.% Ti₃C₂	114.08	139.40

Based on these data, the values of E_a of the first-step hydrogen desorption reaction of NaMgH$_3$ and NaMgH$_3$-7 wt.% Ti$_3$C$_2$ are calculated to be 158.45 and 114.08 kJ/mol, respectively. For the second-step reaction, the value of E_a declines from 165.16 to 139.40 kJ/mol by doping with 7 wt.% Ti$_3$C$_2$. The reduction of E_a for both two reactions demonstrates that the improved dehydriding properties of NaMgH$_3$ can be ascribed to the Ti$_3$C$_2$ dopant by reducing the second-step dehydrogenation energy barrier.

The role played by unique lamellar-structure Ti$_3$C$_2$ during the dehydrogenation reactions was researched and explored. Figure 5a,b shows the SEM images of the pure NaMgH$_3$ sample, in which some small particles with average size of approximately 1 μm agglomerate together to form a larger cluster. In Figure 5c, the results of EDS analyses further confirm the results of the XRD measurements noted above, suggesting the successful synthesis of NaMgH$_3$. In contrast, the large layer-structure (about 10 μm wide) of Ti$_3$C$_2$ is completely broken into smaller lamellar-structure (about 2 μm wide) during the ball-milling procedure, with some tiny NaMgH$_3$ particles attached, as shown in Figure 5d,e. Furthermore, after 12 h ball milling, the agglomerated NaMgH$_3$ particles were separated homogeneously by the lamellar-structure Ti$_3$C$_2$. The following EDS analyses (Figure 5f) prove the existence of NaMgH$_3$ and Ti$_3$C$_2$. Based on the significant reduction of operating temperature and the superior enhancement of dehydrogenation kinetics properties in the Ti$_3$C$_2$ doped sample, it can be proposed that Ti$_3$C$_2$ plays the role of catalyst to improve the dehydrogenation kinetics properties of NaMgH$_3$ hydride, which is in agreement with our previous papers in Ti$_3$C$_2$-doped Mg(BH$_4$)$_2$ [33] and sodium alanate systems [34]. Apparently, the exploration of the SEM and EDS results described above indicate that the significant reduction of operating temperature and the superior enhancement of dehydrogenation kinetic properties of the 7 wt.% Ti$_3$C$_2$ doped sample can be mainly due to the unique lamellar-structure. The detailed microstructure information of Ti$_3$C$_2$ could not be easily revealed after the re/dehydrogenation process due to the small amounts of Ti$_3$C$_2$ additive; thus, the catalytic mechanism remains undiscovered. We hope that the catalytic mechanism of NaMgH$_3$-x wt.% Ti$_3$C$_2$ composite can be revealed in the future by a X-ray absorption near-edge structure (XANES) spectrum.
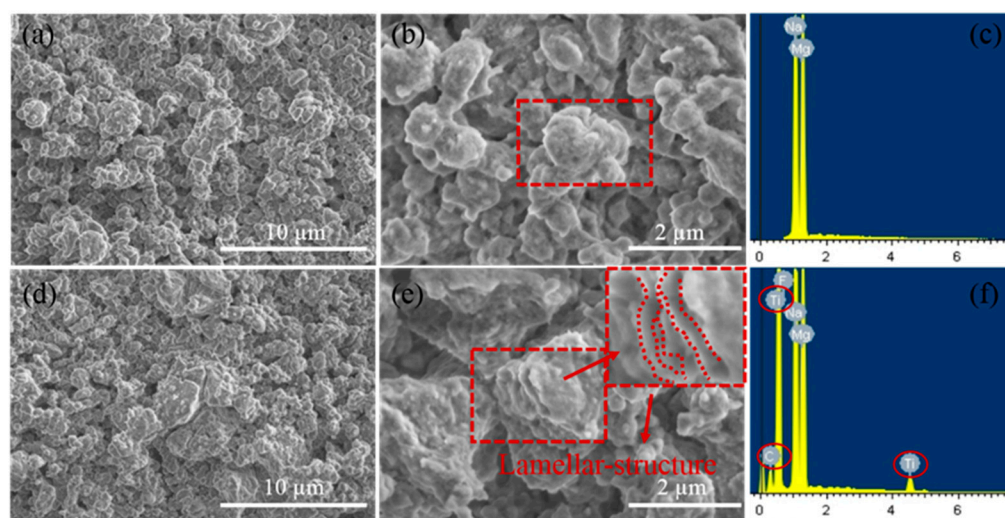
Figure 5. SEM images of (**a**,**b**) NaMgH$_3$ and (**d**,**e**) NaMgH$_3$-7 wt.% Ti$_3$C$_2$; EDS results of (**c**) NaMgH$_3$ and (**f**) NaMgH$_3$-7 wt.% Ti$_3$C$_2$.

Figure 6 shows the isothermal hydrogenation curves of pure NaMgH$_3$ and NaMgH$_3$-7 wt.% Ti$_3$C$_2$ samples at different temperatures. It is obvious that the hydrogen absorption kinetics of NaMgH$_3$ can be enhanced by doping with Ti$_3$C$_2$, resulting in the high capacity achieved at the same hydrogenation condition. Figure 6a shows the isothermal hydrogenation curves of pure NaMgH$_3$ and NaMgH$_3$-7 wt.% Ti$_3$C$_2$ samples at 300 °C. The 7 wt.% Ti$_3$C$_2$-containing composite can quickly absorb approximately 3.5 wt.% H$_2$ within 6 s.

However, the pure NaMgH$_3$ displays unacceptably slow re-hydrogenation kinetics, storing 3.0 wt.% H$_2$ in 15 min. This result suggests that only the first-step hydrogenation reaction is thermodynamically available at 300 °C. As the hydrogenation temperature increases to 350 °C, the hydrogenation kinetics of two dehydrogenated samples are improved, approximately 3.8 and 4.3 wt.% H$_2$ stored for NaMgH$_3$ and NaMgH$_3$-7 wt.% Ti$_3$C$_2$ samples, respectively. The results reveal that first- and second-step hydrogenation reactions of the samples are feasible in thermodynamics, as the temperature increases to 350 °C. However, the second-step hydrogenation kinetics of both samples are too slow to desorb more hydrogen within 30 min. When the hydrogenation temperature rises to 400 °C, the Ti$_3$C$_2$-containing sample exhibits excellent hydrogenation kinetics, absorbing 4.9 wt.% H$_2$ in 8 min, confirming that the first- and second-step hydrogen absorption kinetics have been further improved. The hydrogenation capacity of pure NaMgH$_3$ is found to be 4.2 wt.% H$_2$ in 15 min, with the second-step hydrogen absorption kinetics still being sluggish. In summary, Ti$_3$C$_2$ has obvious catalytic efficiency on the enhancement of both first- and second-step hydrogenation kinetic properties of NaMgH$_3$ under 80 bar H$_2$ at 300, 350, and 400 °C.
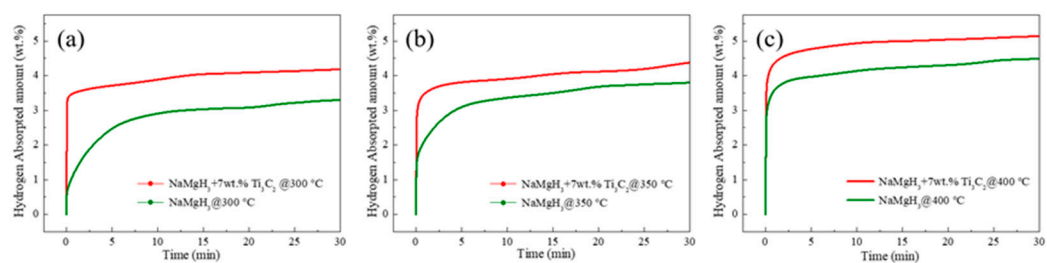
Figure 6. Isothermal hydrogenation curves of pure NaMgH3 and NaMgH3-7 wt.% Ti3C2 at different temperatures. (**a**) 300 °C (**b**) 350 °C (**c**) 400 °C.

The reversible dehydrogenation properties of NaMgH$_3$ are remarkably enhanced because of the superior catalytic activity of Ti$_3$C$_2$ with lamellar-structure. To obtain the cycling properties of NaMgH$_3$ with or without dopant, the cycling isothermal dehydrogenation curves and hydrogen capacities of two samples are displayed in Figure 7. In the first cycle, pure NaMgH$_3$ desorbs 5.5 wt.% H$_2$ in 15 min at 400 °C. After hydrogenation at 400 °C under 60 bar H$_2$, it releases only 2.6 wt.% H$_2$ in 60 min, losing approximately half of its initial capacity. The dehydrogenation kinetic property of pure NaMgH$_3$ also suffers tremendous degradation in the second cycle, especially in the latter 3rd, 4th and 5th cycles, 3.8, 4.0, and 3.75 wt.% H$_2$ were desorbed in 20 min, respectively. The dehydrogenation kinetics and capacity of pure NaMgH$_3$ in the latter three cycles are recovered from the poor second cycle. For the Ti$_3$C$_2$ doped NaMgH$_3$, in the first cycle, about 5.1 wt.% H$_2$ is released in 5 min. The difference is that the Ti$_3$C$_2$ doped sample does not suffer tremendous capacity loss in the second cycle. In the latter four cycles, the Ti$_3$C$_2$ doped sample desorbs 4.3, 4.4, 4.4, and 4.6 wt.% H$_2$ in 20 min, respectively. In five cycles, pure NaMgH$_3$ suffers a huge capacity loss from 5.5 to 4.1 wt.% H$_2$, losing a quarter of its initial capacity. It is well known that a material with faster kinetics will release more hydrogen within a fixed time. Hence, Ti$_3$C$_2$ can relieve the degradation of dehydrogenation capacity to some extent due to its improved dehydrogenation kinetics. However, it is clear that the lamellar-structure Ti$_3$C$_2$ can effectively enhance the cycling stability of NaMgH$_3$ in five cycles. The expectation of the dehydrogenation kinetics and cycling stability of NaMgH$_3$ remaining unchanged is not achieved. Therefore, further investigation of enhancing the cycle stability of NaMgH$_3$ should be explored.
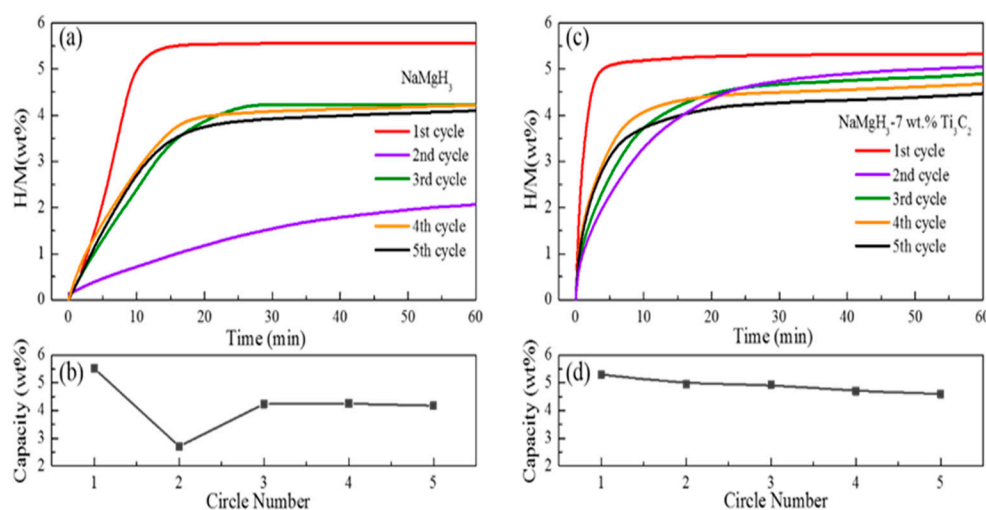
Figure 7. Isothermal dehydrogenation cycle curves of (**a**) NaMgH$_3$ and (**c**) NaMgH$_3$-7 wt.% Ti$_3$C$_2$ at 400 °C; cycle capacity curves of (**b**) NaMgH$_3$ and (**d**) NaMgH$_3$-7 wt.% Ti$_3$C$_2$.

The pronounced degradation of dehydrogenation performance and hydrogen capacity in the second cycle for the pure NaMgH$_3$ is abnormal. There should be some phase separations during hydrogenation after the first cycle dehydrogenation. Furthermore, it was found that pure NaMgH$_3$ would segregate into separate NaH and Mg during the high-temperature cycling tests [39]. In order to confirm the phase transformation of Ti$_3$C$_2$ doped/undoped NaMgH$_3$ samples during hydrogen storage process, XRD characterization was carried out for the re-hydrogenated sample. In Figure 8a,b, the NaMgH$_3$, NaH, Mg, and MgO phases can be seen in the XRD patterns of the pure NaMgH$_3$ sample after the second and third hydrogenations. The separation of NaH and Mg phases after hydrogenation can explain the reason why abnormal degradation occurs. Therefore, the detailed reaction process can be proposed as follows. When pure NaMgH$_3$ dehydrogenates at 400 °C, both of the two step decomposition reactions occur quickly, forming molten Na and solid Mg. The drastic molten Na covers the outside surface of solid Mg particles to form the compact Na layer so that most Na and Mg are separated; the residual Na would be hydrogenated to form the solid NaH during the subsequent hydrogenation process, which hinders the further absorption of H$_2$, making the formation of MgH$_2$ and NaMgH$_3$ much more difficult, thereby decreasing the hydrogen capacity of NaMgH$_3$ [37]. Therefore, the formation of the NaH layer must be responsible for the pronounced degradation of dehydrogenation performance in the second cycle for the pure NaMgH$_3$. This hypothesis can be proved by the strong diffraction peaks of NaH in the second hydrogenation sample (Figure 8). Moreover, the enhanced dehydrogenation performance of the pure NaMgH$_3$ sample in the latter three cycles would be due to the distillation of molten Na making the NaH layer thinner [37]. In contrast, the XRD patterns of the hydrogenated NaMgH$_3$-7 wt.% Ti$_3$C$_2$ sample displays the diffraction peaks of NaMgH$_3$, MgH$_2$, and MgO, without any diffraction peaks belonging to NaH (Figure 8c,d). The weak diffraction peaks of MgH$_2$ are caused by the distillation of molten Na during the cycles. Meanwhile, to confirm the separation phenomenon of Na and Mg, the dehydrogenation processes at 400 °C can be observed through a homemade quartz tube. It can be observed that after hydrogenation the pure NaMgH$_3$ appears as a light-yellow metal layer ingoting with metallic luster, corresponding to the existence of NaH (Figure S1a,b). However, the deposition of NaH disappears in the Ti$_3$C$_2$-doped NaMgH$_3$ sample (Figure S1c,d). Herein, the XRD results and dehydrogenation observation indicate that the existence of lamellar-structure Ti$_3$C$_2$ can effectively prevent Na from separating Mg to form the insular NaH layer, largely preserving the cycling dehydrogenation properties of NaMgH$_3$.
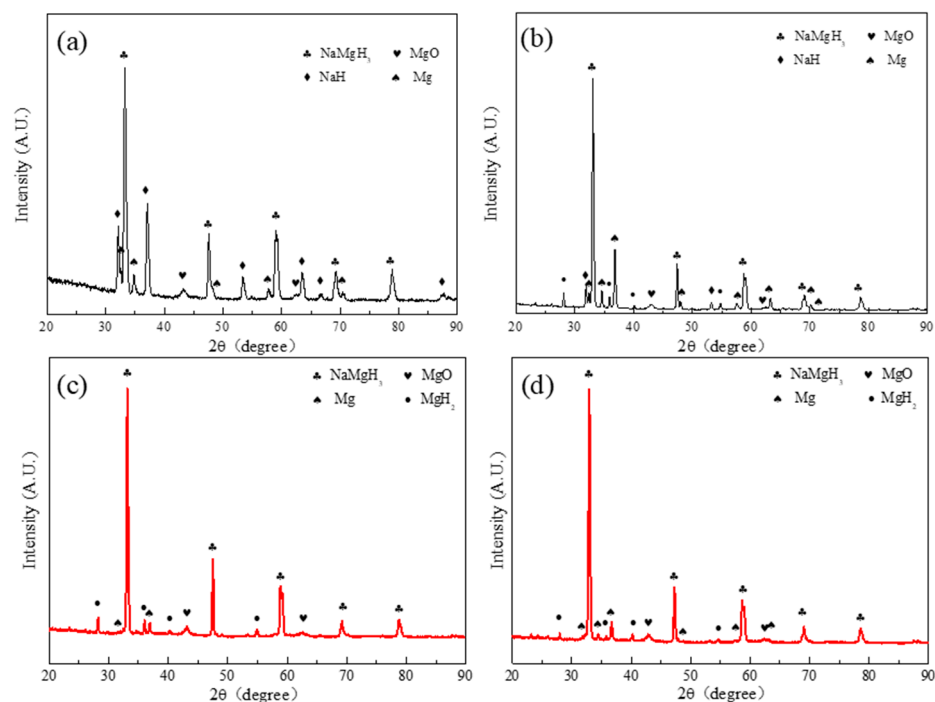
Figure 8. XRD patterns of pure $NaMgH_3$ before the (**a**) second and (**b**) third dehydrogenations at 400 °C. XRD patterns of $NaMgH_3$-7 wt.% Ti_3C_2 before the (**c**) second and (**d**) third dehydrogenations at 400 °C.

In addition to its use as a hydrogen storage application, $NaMgH_3$ can also be a potential candidate for thermal energy storage (TES) owing to the theoretical thermal storage density as high as 2881 kJ/kg [37]. In Figure S2a,b, the thermal storage densities of as-formed pure $NaMgH_3$ and $NaMgH_3$-7 wt.% Ti_3C_2 samples are calculated to be 2727 and 2562 kJ/kg through DSC profiles, respectively. The reduction of ~6.0% thermal storage density for the $NaMgH_3$-7 wt.% Ti_3C_2 sample is mainly due to the dead weight of Ti_3C_2 and existence of MgO. Even with this reduction, as-formed $NaMgH_3$-7 wt.% Ti_3C_2 sample exceeds the thermal storage properties of most other candidates (Table 2). Meanwhile, Ti_3C_2 dramatically enhances the de/re-hydrogenation kinetics and cycling performance of $NaMgH_3$, making it more suitable for TES application [40].

Table 2. Thermal energy storage densities of different thermochemical energy storage materials [41–44].

Type of Thermal Energy Storage (TES)	Example of TES Materials	Total Thermal Storage Capacity (kJ/kg)
Sensible heat	Molten salt mixtures	153 *
Latent heat/phase change materials	$NaNO_3$	282 *
Thermochemical	Oxidation of Co_3O_4	1055 *
	$NaMgH_3$-7 wt.% Ti_3C_2	2562
Metal hydrides	$NaAlH_4$	711 *
	Mg_2NiH_4	1157 *
	Mg_2FeH_6	2090 *

* Theoretical thermal storage capacity.

4. Conclusions

$NaMgH_3$ is considered a potential candidate for hydrogen storage and thermal storage, but further practical applications are limited by its poor de/re-hydrogenation kinetics

and cycling performance. An investigation of enhancing the re/dehydrogenation kinetics and cycling performance of $NaMgH_3$ through doping with Ti_3C_2 was carried out by using XRD, SEM, TPD, DSC, isothermal de/re-hydrogenation measurements and cycling tests. The $NaMgH_3$-7 wt.% Ti_3C_2 sample exhibits the optimal dehydrogenation performance, reducing the two-step desorption peak temperatures from 372.3 and 380.3 °C to 324.8 and 345.3 °C, respectively. The $NaMgH_3$-7 wt.% Ti_3C_2 can release 4.8 wt.% H_2 in 15 min and 3.4 wt.% H_2 in 5 min at 365 °C and 350 °C, respectively. The unique lamellar-structure of Ti_3C_2 can separate the agglomerated $NaMgH_3$ particles homogeneously and decrease the activation energy of $NaMgH_3$ to 114.08 and 139.4 kJ/mol for the first- and second-step dehydrogenation reactions, respectively. The addition of Ti_3C_2 also dramatically enhances the hydrogen storage kinetics of $NaMgH_3$ at 300, 350, and 400 °C. Approximately 3.5 wt.% H_2 is absorbed in 6 s for the $NaMgH_3$-7 wt.% Ti_3C_2 sample at 300 °C. The poor cycling properties of $NaMgH_3$ are improved by Ti_3C_2, with 4.6 wt.% H_2 capacity remaining after five cycles. Lamellar-structure Ti_3C_2 can homogeneously separate aggregated $NaMgH_3$ particles and prevent Na from separating Mg after dehydrogenation. Furthermore, $NaMgH_3$-7 wt.% Ti_3C_2 with its high thermal storage density of 2562 kJ/kg and fast kinetics can be a potential candidate for TES.

Supplementary Materials: The following are available online at www.mdpi.com/article/10.3390/pr9101690/s1, Figure S1: Photographs of pure $NaMgH_3$ and $NaMgH_3$-7 wt.% Ti_3C_2 (a and c) before and (b and d) after dehydrogenation at 400 °C. Figure S2: DSC profiles of (a) pure $NaMgH_3$ and (b) $NaMgH_3$-7 wt.% Ti_3C_2 at a heating rate of 5 °C/min.

Author Contributions: The experimental work, original draft preparation, and modification, Z.H. (Zhouming Hang) and Z.H. (Zhencan Hu); methodology for experiments, manuscript review, and editing, X.X. and R.J.; conceptualization and data analysis, resources, project administration, and funding acquisition, X.X.; data analysis, M.Z. All authors have read and agreed to the published version of the manuscript.

Conflicts of Interest: The authors declare no conflict of interest.

References

1. Santos, D.M.F.; Sequeira, C.A.C. Sodium borohydride as a fuel for the future. *Renew. Sust. Energ. Rev.* **2011**, *15*, 3980–4001.
2. Ahluwalia, R.K. Sodium alanate hydrogen storage system for automotive fuel cells. *Int. J. Hydrogen Energy* **2007**, *32*, 1251–1261.
3. Liu, Y.; Wang, S.; Li, Z.; Gao, M.; Liu, Y.; Sun, W.; Pan, H. Enhanced hydrogen storage performance of MgH_2 by the catalysis of a novel Intersected Y_2O_3/NiO hybrid. *Processes* **2021**, *9*, 892.
4. Hu, Z.C.; Qin, H.Y.; Xiao, X.Z.; Chen, M.; Liu, M.J.; Jiang, R.C.; Chen, L.X. Excellent catalysis of various TiO_2 dopants with $Na_{0.46}TiO_2$ in situ formed on the enhanced dehydrogenation properties of $NaMgH_3$. *J. Phys. Chem. C* **2019**, *123*, 22832–22841.
5. Zhang, X.; Liu, Y.; Ren, Z.; Zhang, X.; Hu, J.; Huang, Z.; Lu, Y.; Gao, M.; Pan, H. Realizing 6.7 wt% reversible storage of hydrogen at ambient temperature with non-confined ultrafine magnesium hydrides. *Energy Environ. Sci.* **2021**, *14*, 2302–2313.
6. Huang, X.; Xiao, X.; He, Y.; Yao, Z.; Ye, X.; Kou, H.; Chen, C.; Huang, T.; Fan, X.; Chen, L. Probing an intermediate state by X-ray absorption near-edge structure in nickel-doped $2LiBH_4$–MgH_2 reactive hydride composite at moderate temperature. *Mater. Today Nano* **2020**, *12*, 100090.
7. Poupin, L.; Humphries, T.D.; Paskevicius, M.; Buckley, C.E. A thermal energy storage prototype using sodium magnesium hydride. *Sustain. Energy Fuels* **2019**, *3*, 985–995.
8. Chen, W.; Xiao, X.; He, J.; Dong, Z.; Wang, X.; Chen, M.; Chen, L. A dandelion-like amorphous composite catalyst with outstanding performance for sodium borohydride hydrogen generation. *Int. J. Hydrogen Energy* **2021**, *46*, 10809–10818.
9. Reshak, A.H. $NaMgH_3$ a perovskite-type hydride as advanced hydrogen storage systems: Electronic structure features. *Int. J. Hydrogen Energy* **2015**, *40*, 16383–16390.
10. Ikeda, K.; Kogure, Y.; Nakamori, Y.; Orimo, S. Reversible hydriding and dehydriding reactions of perovskite-type hydride $NaMgH_3$. *Scr. Mater.* **2005**, *53*, 319–322.
11. Bouamrane, A.; Laval, J.P.; Soulie, J.P.; Bastide, J.P. Structural characterization of $NaMgH_2F$ and $NaMgH_3$. *Mater. Res. Bull.* **2000**, *35*, 545–549.

12. Wu, H.; Zhou, W.; Udovic, T.J.; Rush, J.J.; Yildirim, T. Crystal chemistry of perovskite-type hydride NaMgH$_3$: Implications for hydrogen storage. *Chem. Mater.* **2008**, *20*, 2335–2342.

13. Pottmaier, D.; Pinatel, E.R.; Vitillo, J.G.; Garroni, S.; Orlova, M.; Baró, M.D.; Vaughan, G.B.M.; Fichtner, M.; Lohstroh, W.; Baricco, M. Structure and Thermodynamic Properties of the NaMgH$_3$ Perovskite: A Comprehensive Study. *Chem. Mater.* **2011**, *23*, 2317–2326.

14. Bouhadda, Y.; Fenineche, N.; Boudouma, Y. Hydrogen storage: Lattice dynamics of orthorhombic NaMgH$_3$. *Phys. B Condens. Matter* **2011**, *406*, 1000–1003.

15. Wang, Z.; Tao, S.; Li, J.J.; Deng, J.Q.; Zhou, H.; Yao, Q. The Improvement of Dehydriding the Kinetics of NaMgH$_3$ Hydride via Doping with Carbon Nanomaterials. *Metals* **2017**, *7*, 9.

16. Sheppard, D.; Paskevicius, M.; Buckley, C.E. Thermodynamics of hydrogen desorption from NaMgH$_3$ and its application as a solar heat storage medium. *Chem. Mater.* **2011**, *23*, 4298–4300.

17. Wang, Z.; Li, J.J.; Tao, S.; Deng, J.Q.; Zhou, H.; Yao, Q. Structure, thermal analysis and dehydriding kinetic properties of Na$_{1-x}$Li$_x$MgH$_3$ hydrides. *J. Alloys Compd.* **2015**, *660*, 402–406.

18. Tao, S.; Wang, Z.M.; Wan, Z.Z.; Deng, J.Q.; Zhou, H.; Yao, Q. Enhancing the dehydriding properties of perovskite-type NaMgH$_3$ by introducing potassium as dopant. *Int. J. Hydrogen Energy* **2017**, *42*, 3716–3722.

19. Li, Y.; Zhang, L.; Zhang, Q.; Fang, F.; Sun, D.; Li, K.; Wang, H.; Ouyang, L.; Zhu, M. In situ embedding of Mg$_2$NiH$_4$ and YH$_3$ nanoparticles into bimetallic hydride NaMgH$_3$ to inhibit phase segregation for enhanced hydrogen storage. *J. Phys. Chem. C* **2014**, *118*, 22635–23644.

20. Wang, Z.; Tao, S.; Deng, J.; Zhou, H.; Yao, Q. Significant improvement in the dehydriding properties of perovskite hydrides, NaMgH$_3$, by doping with K$_2$TiF$_6$. *Int. J. Hydrogen Energy* **2017**, *42*, 8554–8559.

21. Ismail, M.; Zhao, Y.; Yu, X.B.; Dou, S.X. Improved hydrogen storage performance of MgH$_2$–NaAlH$_4$ composite by addition of TiF$_3$. *Int. J. Hydrogen Energy* **2012**, *37*, 8395–8401.

22. Alhabeb, M.; Maleski, K.; Anasori, B.; Lelyukh, P.; Clark, L.; Sin, S.; Gogotsi, Y. Guidelines for synthesis and processing of 2D titanium carbide (Ti$_3$C$_2$T$_x$ MXene). *Chem. Mater.* **2017**, *29*, 7633–7644.

23. Yang, J.; Chen, B.; Song, H.; Tang, H.; Li, C. Synthesis, characterization, and tribological properties of two-dimensional Ti$_3$C$_2$. *Cryst. Res. Technol.* **2014**, *49*, 926–932.

24. Naguib, M.; Kurtoglu, M.; Presser, V.; Lu, J.; Niu, J.; Heon, M.; Hultman, L.; Gogotsi, Y.; Barsoum, M. Two-Dimensional Nanocrystals: Two-dimensional nanocrystals produced by exfoliation of Ti$_3$AlC$_2$. *Adv. Mater.* **2011**, *23*, 4248–4253.

25. Lin, H.; Wang, Y.; Gao, S.; Chen, Y.; Shi, J. Theranostic 2D tantalum carbide (MXene). *Adv. Mater.* **2017**, *30*, 1703284.

26. Anasori, B.; Lukatskaya, M.; Gogotsi, Y. 2D metal carbides and nitrides (MXenes) for energy storage. *Nat. Rev. Mater.* **2017**, *2*, 1–17.

27. Naguib, M.; Mashtalir, O.; Lukatskaya, M.; Dyatkin, B.; Zhang, C.; Presser, V.; Gogotsi, Y.; Barsoum, M. One-step synthesis of nanocrystalline transition metal oxides on thin sheets of disordered graphitic carbon by oxidation of MXenes. *Chem. Commun.* **2014**, *50*, 7420–7423.

28. Naguib, M.; Halim, J.; Lu, J.; Cook, K.M.; Hultman, L.; Gogotsi, Y.; Barsoum, M.W. New two-dimensional niobium and vanadium carbides as promising materials for Li-ion batteries. *J. Am. Chem. Soc.* **2013**, *135*, 15966–15969.

29. Wu, R.; Du, H.; Wang, Z.; Gao, M.; Pan, H.; Liu, Y. Remarkably improved hydrogen storage properties of NaAlH$_4$ doped with 2D titanium carbide. *J. Power Sources* **2016**, *327*, 519–525.

30. Liu, Y.; Du, H.; Zhang, X.; Yang, Y.; Gao, M.; Pan, H. Superior catalytic activity derived from two-dimensional Ti$_3$C$_2$ precursor towards the hydrogen storage reaction of magnesium hydride. *Chem. Commun.* **2015**, *52*, 705–708.

31. Fan, X.; Zhang, Y.; Zhu, Y.; Guo, X.; Chen, J.; Li, L. Hydrogen storage performances and reaction mechanism of non-stoichiometric compound Li$_{1.3}$Na$_{1.7}$AlH$_6$ doped with Ti$_3$C$_2$. *Chem. Phys.* **2018**, *513*, 135–140.

32. Cheng, H.; Li, K.; Fan, X.; Lou, H.; Liu, Y.; Qi, Q.; Zhang, J.; Liu, J.; Yan, K.; Zhang, Y. The enhanced de/re-hydrogenation performances of LiNa$_2$AlH$_6$ combined with two-dimension lamellar Ti$_3$C$_2$. *Int. J. Hydrogen Energy* **2017**, *42*, 25285–25293.

33. Zheng, J.G.; Cheng, H.; Xiao, X.Z.; Chen, M.; Chen, L.X. Enhanced low temperature hydrogen desorption properties and mechanism of Mg(BH$_4$)$_2$ composited with 2D MXene. *Int. J. Hydrogen Energy* **2019**, *44*, 24292–24300.

34. Jiang, R.; Xiao, X.; Zheng, J.; Chen, M.; Chen, L. Remarkable hydrogen absorption/desorption behaviors and mechanism of sodium alanates in-situ doped with Ti-based 2D MXene. *Mater. Chem. Phys.* **2020**, *242*, 122529.

35. Yartys, V.A.; Lototskyy, M.V.; Akiba, E.; Albert, R.; Antonov, V.E.; Ares, J.R.; Baricco, M.; Bourgeois, N.; Buckley, C.E.; Bellosta von Colbe, J.M.; et al. Magnesium based materials for hydrogen based energy storage: Past, present and future. *Int. J. Hydrogen Energy* **2019**, *44*, 7809–7859.

36. He, T.; Pachfule, P.; Wu, H.; Xu, Q.; Chen, P. Hydrogen carriers. *Nat. Rev. Mater.* **2016**, *1*, 1–17.

37. Sheppard, D.A.; Humphries, T.D.; Buckley, C.E. Sodium-based hydrides for thermal energy applications. *Appl. Phys. A* **2016**, *122*, 406.

38. Kissinger, H.E. Reaction kinetics in differential thermal analysis. *Anal. Chem.* **1957**, *29*, 1702–1706.

39. Ward, P.A.; Corgnale, C.; Teprovich, J.A.; Motyka, T.; Hardy, B.; Peters, B.; Zidan, R. High performance metal hydride based thermal energy storage systems for concentrating solar power applications. *J. Alloys Compd.* **2015**, *645*, S374–S378.

40. Aydin, D.; Casey, S.P.; Riffat, S. The latest advancements on thermochemical heat storage systems. *Renew. Sust. Energ. Rev.* **2015**, *41*, 356–367.

41. Harries, D.; Paskevicius, M.; Sheppard, D.; Edward Cameron Price, T.; Buckley, C.E. Concentrating solar thermal heat storage using metal hydrides. *Proc. IEEE* **2012**, *100,* 539–549.
42. Fellet, M.; Buckley, C.E.; Paskevicius, M.; Sheppard, D.A.; Research on metal hydrides revived for next-generation solutions to renewable energy storage. *MRS Bull.* **2013**, 38, 1012-1013.
43. Sheppard, D.A.; Corgnale, C.; Hardy, B.; Motyka, T.; Zidan, R.; Paskevicius, M.; Buckley, C.E. Hydriding characteristics of NaMgH$_2$F with preliminary technical and cost evaluation of magnesium-based metal hydride materials for concentrating solar power thermal storage. *RSC Adv.* **2014**, 4, 26552-26562.
44. Paskevicius, M.; Sheppard, D.A.; Williamson, K.; Buckley, C.E. Metal hydride thermal heat storage prototype for concentrating solar thermal power. *Energy* **2015**, *88*, 469–477.

经检索《Web of Science》和《Journal Citation Reports（JCR）》数据库，《Science Citation Index Expanded (SCI-EXPANDED)》收录论文及其期刊影响因子、分区情况如下。（检索时间：2021 年 12 月 9 日）

第 1 条，共 1 条

标题:Enhancing Hydrogen Storage Kinetics and Cycling Properties of NaMgH3 by 2D Transition Metal Carbide MXene Ti3C2

作者:Hang, ZM(Hang, Zhouming);Hu, ZC(Hu, Zhencan);Xiao, XZ(Xiao, Xuezhang);Jiang, RC(Jiang, Ruicheng);Zhang, M(Zhang, Meng);

来源出版物:PROCESSES 卷:9 期:10 文献号:1690 DOI:10.3390/pr9101690 出版年:OCT 2021

入藏号:WOS:000716993200001

文献类型:Article

地址:

[Hang, Zhouming] Zhejiang Univ Water Resources & Elect Power, Coll Mech & Automot Engn, Hangzhou 310018, Peoples R China.

[Hang, Zhouming] Zhejiang Univ Water Resources & Elect Power, Zhejiang Engn Res Ctr Adv Hydraul Equipment, Hangzhou 310018, Peoples R China.

[Hang, Zhouming] Zhejiang Univ Water Resources & Elect Power, Key Lab Technol Rural Water Management Zhejiang P, Hangzhou 310018, Peoples R China.

[Hu, Zhencan; Xiao, Xuezhang; Jiang, Ruicheng; Zhang, Meng] Zhejiang Univ, Sch Mat Sci & Engn, State Key Lab Silicon Mat, Hangzhou 310027, Peoples R China.

通讯作者地址:

Xiao, XZ (corresponding author), Zhejiang Univ, Sch Mat Sci & Engn, State Key Lab Silicon Mat, Hangzhou 310027, Peoples R China.

电子邮件地址:hangzhm@zjweu.edu.cn; 21726113@zju.edu.cn; xzxiao@zju.edu.cn;21726011@zju.edu.cn; 11726062@zju.edu.cn

IDS 号:WV1JL

eISSN:2227-9717

期刊《PROCESSES》2020 年的影响因子为 **2.847**，五年影响因子为 **2.824**。

期刊《PROCESSES》2020 年的 JCR 分区情况为：

Edition	JCR® 类别	类别中的排序	JCR 分区
SCI	ENGINEERING, CHEMICAL	**74/143**	**Q3**

注：

1. 期刊影响因子及分区情况最新数据以 JCR 数据库最新数据为准。
2. 以上检索结果来自 CALIS 查收查引系统。
3. 以上检索结果均得到委托人及被检索作者的确认。

教育部科技查新工作站（Z09）

检索人（签章）：王卓

2021 年 12 月 9 日